Physica D 349 (2017) 12–26

Contents lists available at ScienceDirect

Physica D

journal homepage: www.elsevier.com/locate/physd

Stability of the phase motion in race-track microtrons☆

Yu.A. Kubyshin [a], O. Larreal [b], R. Ramírez-Ros [c,*], T.M. Seara [c]

[a] Institut de Tècniques Energètiques, Universitat Politècnica de Catalunya, Diagonal 647, 08028 Barcelona, Spain
[b] Departamento de Matemáticas, Universidad del Zulia, Maracaibo, Venezuela
[c] Departament de Matemàtiques, Universitat Politècnica de Catalunya, Diagonal 647, 08028 Barcelona, Spain

HIGHLIGHTS

- The stability of phase oscillations of electrons in race-track microtrons is studied.
- The phase oscillations are modeled by means of an area preserving map.
- Our numerical study agrees with two known empirical rules of particle accelerators.

ARTICLE INFO

Article history:
Received 12 September 2016
Accepted 2 March 2017
Available online 18 March 2017
Communicated by B. Sandstede

Keywords:
Stability domain
Invariant curve
Hamiltonian approximation
Exponentially small phenomena
Microtron

ABSTRACT

We model the phase oscillations of electrons in race-track microtrons by means of an area preserving map with a fixed point at the origin, which represents the *synchronous trajectory* of a reference particle in the beam. We study the nonlinear stability of the origin in terms of the *synchronous phase* —the phase of the synchronous particle at the injection. We estimate the size and shape of the stability domain around the origin, whose main connected component is enclosed by an invariant curve. We describe the evolution of the stability domain as the synchronous phase varies. We also clarify the role of the stable and unstable invariant curves of some hyperbolic (fixed or periodic) points.

1. Introduction

Race-track microtron (RTM) is a specific type of electron accelerator with beam recirculation combining properties of the linear accelerator and a circular machine [1,2]. For applications in which a modest beam power at a relatively high beam energy is required the RTM turns out to be the most optimal source of electron beams. This is the case of applications like the cargo inspection or Intraoperative Radiation Therapy for which RTMs allow to get pulsed and continuous beams in a quite cost and energy effective way with the most optimal dimensions of the machine. An example of such accelerator is a compact 12 MeV RTM which is under construction at the Technical University of Catalonia in collaboration with the Moscow State University and CIEMAT (Spain) [3–5].

In the design of a particle accelerator its main parameters are optimized for some reference particle, usually referred to as synchronous particle. Real particles of the beam perform transverse and longitudinal oscillations with respect to this synchronous particle. One of the important issues of the RTM design is to assure the stability of these oscillations, in particular to avoid an uncontrolled growth of their amplitude that leads to the loss of the beam. In the RTM beam dynamics the main role is played by longitudinal oscillations of individual electrons with respect to the synchronous particle [6,7]. Such oscillations are usually referred to as phase motion, and the region of initial states in the phase space which give rise to stable oscillations is called *acceptance*.

Stability of the phase oscillations of particles in the beam is a matter of primary concern both at the stage of the accelerator design and during its operation. In particular, the size of the acceptance determines the efficiency of caption into acceleration of particles injected from a source of electrons, usually an electron

☆ Research supported in part by MINECO-FEDER grant MTM2015-65715-P (Spain) and CUR-DIUE grants 2014SGR504 and 2014SGR846 (Catalonia). T. M. Seara is also supported by the Russian Scientific Foundation grant 14-41-00044 and the European Marie Curie Action FP7-PEOPLE-2012-IRSES: BREUDS. We acknowledge the use of the UPC Applied Math cluster system for research computing. Useful conversations with Amadeu Delshams, Vasiliy Shvedunov, and Arturo Vieiro are gratefully acknowledged. We also thank the anonymous referee that pointed out reference (Fox and de la Llave, 2015).

* Corresponding author.
E-mail addresses: Iouri.Koubychine@upc.edu (Yu.A. Kubyshin), olarreal@luz.edu.ve (O. Larreal), Rafael.Ramirez@upc.edu (R. Ramírez-Ros), Tere.M.Seara@upc.edu (T.M. Seara).

http://dx.doi.org/10.1016/j.physd.2017.03.001
0167-2789/

gun. The shape and size of the acceptance depend on the phase of the synchronous particle, also called synchronous phase and denoted as ϕ_s in this paper. The definition of these notions will be given in Section 2. A specific feature of the RTM is that the range of values of ϕ_s for which the acceptance exists is quite narrow and therefore this parameter must be carefully chosen and controlled during the RTM operation. The main criteria here is to keep the synchronous phase equal or close to the value for which the size of the acceptance is maximal and to avoid resonant values of ϕ_s. The latter is important because resonant phase oscillations lead to a buildup of beam instabilities, rapid growth of the amplitude of the phase oscillations and eventually to a loss of the beam. Therefore, a good understanding of the longitudinal dynamics of the beam in RTMs in general and the phase oscillations of electrons in a particular machine is important.

The phase oscillations of the beam in an RTM are described by a system of nonlinear difference equations [8,2] that will be derived in Section 2. It gives rise to an analytic area preserving map which is the object of study in the present paper. These difference equations cannot be approximated by differential equations without loss of accuracy, since RTMs have large energy gain per turn and high frequency of phase oscillations. The description of the acceptance in the linear approximation is well known [2]. The change of the acceptance under the variation of the synchronous phase, the appearance of stable regions, and the emergence of the stochastic regime is studied in [9] by looking at the normal form of the difference equations up to order four. For instance, it was shown that there is a shift of the center of oscillations and that the oscillation frequency depends on the amplitude. We will reproduce these known results.

In the present paper we will study the phase motion of the beam in RTMs using modern dynamical systems methods. Our goal is to characterize the acceptance, called stability domain in dynamical systems, as a function of the synchronous phase. In particular, we will establish the intervals of values of ϕ_s for which the acceptance and its central connected component exist, analyze their geometry, shape and size, and calculate their area for the whole range of ϕ_s. Our main theoretical tools are the Moser twist theorem and several of Simó's stability results [10]. Finally, we will carry out a global study of the acceptance and its connected component using results and algorithms, like the orbit method, developed in [11,12].

The article is organized as follows. We give a short introduction into the RTM beam longitudinal dynamics, define the notion of synchronous trajectory and synchronous phase and derive the map describing the longitudinal beam dynamics that we will refer to as RTM map in Section 2. We present some preliminaries on the RTM map in Section 3, where we also relate the RTM map with the nonzero flux area preserving map studied in [13]. We summarize our analytical results in Section 4, but we relegate all technical proofs to the appendices. The stability domain is numerically studied in Section 5. The invariant curves of some hyperbolic points are analyzed in Section 6. We discuss our results and present some conclusions in Section 7.

2. The RTM model

The operation of a race-track microtron (RTM) is illustrated in Fig. 1. The initial beam is injected from an electron source (electron gun or external pre-accelerator) into an accelerating structure (AS) consisting of a few resonant cavities. The longitudinal electric component of a high frequency electromagnetic wave (usually a standing wave) accelerates the electrons in the AS. Then the beam is bent by the magnetic field of a 180° bending magnet, called *end magnet*, travels through a free space, usually referred to as *drift space*, follows along a circular trajectory inside the second end magnet and returns to the AS. In this way the beam makes a

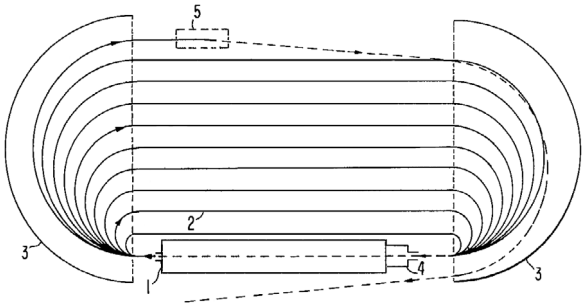

Fig. 1. Schematic view of our RTM model: (1) Accelerating structure, (2) drift space, (3) end magnets, (4) electron gun, and (5) extraction magnet.

number of recirculations through the RTM with the energy being increased at each pass through the AS. Once the beam gets the final design energy, it is deflected by an extraction magnet and is directed towards the accelerator beam exit.

We approximate the AS by a zero length accelerating gap and consider a stationary regime with a constant amplitude of the accelerating field. Then the energy gain of an electron passing through the AS is equal to $\Delta_{\max}\cos\phi$, where $\Delta_{\max}$ is the maximum energy gain in the AS and ϕ is the phase of the accelerating field. In accelerator physics this parameter is usually referred to as particle phase and is used to characterize the longitudinal position of the particle along the orbit with respect to the accelerating gap (in a real machine with respect to, say, the exit, of the last cavity of the AS in the direction of the beam motion). Another idealization in our study is that the end magnets will be considered as hard-edge dipole magnets so that the fringe-field effects are not taken into account.

Let us consider the longitudinal (phase) motion of electrons in an RTM with magnetic field induction B in the end magnets and separation l between the magnets (straight section length). We assume that the injected electrons are already ultra-relativistic, so that in the formulas below the velocity of the particles in the beam is equal to the velocity of light c.

Our dynamical variables are the full particle energy E_n and its phase ϕ_n at the nth turn at some point of the orbit. For the sake of convenience, we choose this point to be the exit of the AS. Let ϕ_0 and E_0 be the particle phase and energy at the injection; that is, just before its first passage through the AS. We would like to note that, in some pulsed RTM, the electrons reverse their trajectory in special reverse field magnets after the injection and first acceleration at the AS [4,5]. In that case, E_0 is the energy after the first acceleration and reflection of the beam in the end magnet, before the second passage through the AS, but we will still use the term injection energy.

For the RTM model described above, the duration of the nth revolution of the beam is

$$T_n = \frac{2l + 2\pi r_n}{c} = \frac{2l}{c} + \frac{2\pi E_n}{ec^2B}, \tag{1}$$

where e is the elementary charge and r_n is the beam trajectory radius in the end magnets. We have used that $E_n = ecBr_n$ in bending magnets for ultrarelativistic beams [2]. Relation (1) allows us to work either with time variables T_n or energy variables E_n. The beam dynamics in the phase-energy variables, for a zero-length AS, is governed by the difference equations

$$\phi_{n+1} = \phi_n + 2\pi T_n/T_{\mathrm{RF}}, \qquad E_{n+1} = E_n + \Delta_{\max}\cos\phi_{n+1}, \tag{2}$$

T_{RF} being the period of the accelerating electromagnetic field, usually called *radiofrequency (RF) field* in the context of accelerator beam dynamics. See [2].

The design of a particle accelerator requires a proper choice of physical and technical parameters in order to guarantee the

existence of a reference trajectory, called *synchronous trajectory*, so that an ideal particle following this trajectory is accelerated in the most optimal way. Namely, it can be tuned in resonance with the accelerating field. Let us explain the choice of parameters in case of an RTM. We fix two positive integers m and k. The resonance conditions in the case of an RTM are

$$\frac{T_{1,s}}{T_{RF}} = m, \qquad \frac{T_{n+1,s} - T_{n,s}}{T_{RF}} = k. \tag{3}$$

Henceforth, the subindex "s" indicates quantities related to the synchronous trajectory. The integer m is the number of RF field periods during the first turn and defines the synchronicity condition at this turn, whereas k is the increase of the multiplicity factor due to the increase of the period of revolution of the reference particle in each turn. The ratio

$$j_n := T_{n,s}/T_{RF} = m + (n-1)k$$

is called *harmonic number*. RTMs are accelerators with variable harmonic numbers, since j_n depends on the nth turn.

If we rewrite the resonance conditions (3) using the energy variables $E_{n,s}$ and relation (1), we get that $E_{n,s} = E_s + n\Delta_s$, where

$$E_s = \left(\frac{m}{k} - 1 - \frac{2l}{k\lambda}\right)\Delta_s, \quad \Delta_s = \frac{ecB\lambda k}{2\pi},$$

and $\lambda = cT_{RF}$ is the wavelength of the RF field. Finally, it is straightforward to check that if the injection phase for the synchronous trajectory $\phi_{0,s} = \phi_{1,s} = \phi_s$ satisfies relation

$$\Delta_s = \Delta_{max} \cos\phi_s,$$

then we get a particular solution $(\phi_{n,s}, E_{n,s})$ of Eqs. (1)–(2), whose energy undergoes a constant gain Δ_s at each turn:

$$\phi_{n,s} = \phi_s + 2\pi i_n, \qquad E_{n,s} = E_s + n\Delta_s, \tag{4}$$

with $i_n = (n-1)m + (n-1)(n-2)k/2$. We note that $i_n \in \mathbb{Z}$, so this synchronous particle passes through the AS in the same phase of the RF field at each turn: $\phi_{n,s} = \phi_s \pmod{2\pi}$ for all n. We say that ϕ_s is the *synchronous phase*.

Once we realize that the synchronous trajectory (4) exists, we wonder whether the oscillations of other trajectories around it are stable. This depends on the synchronous phase ϕ_s.

We study this dependence by introducing the variables

$$\psi_n = \phi_n - \phi_s, \qquad w_n = 2\pi k(E_n - E_{n,s})/\Delta_s, \tag{5}$$

that describe the phase and energy deviation of an arbitrary trajectory from the synchronous one. Then the beam dynamics is modeled by the map $(\psi_{n+1}, w_{n+1}) = f(\psi_n, w_n)$, where

$$\begin{cases} \psi_{n+1} = \psi_n + w_n, \\ w_{n+1} = w_n + 2\pi k\big(\cos(\psi_{n+1} + \phi_s)/\cos\phi_s - 1\big). \end{cases}$$

For simplicity, we will assume that $k = 1$ in the rest of the paper. The study of other values can be carried out in a similar way.

We end this section by stressing that the model of longitudinal oscillations around the synchronous trajectory for non-ultra-relativistic beams is more complicated [14].

3. Fixed points and nonzero flux

Under the assumption $k = 1$, our model for the nonlinear oscillations around the synchronous trajectory (4) is the analytic area preserving diffeomorphism $(\psi_1, w_1) = f(\psi, w)$, defined by

$$\begin{cases} \psi_1 = \psi + w, \\ w_1 = w + 2\pi(\cos\psi_1 - 1) - \mu\sin\psi_1. \end{cases} \tag{6}$$

Here, $\mu = 2\pi\tan\phi_s$ is a parameter, and ψ (respectively, w) is the deviation of the phase (respectively, energy) of an arbitrary particle from the phase (respectively, energy) of the synchronous trajectory. The angular coordinate ψ is defined modulo 2π, so the phase space is $\mathbb{T}\times\mathbb{R}$, with $\mathbb{T} = \mathbb{R}/2\pi\mathbb{Z}$.

The map (6) has two fixed points:

$$p_s = (\psi_s, w_s) = (0,0), \qquad p_h = (\psi_h, w_h) := (-2\phi_s, 0).$$

The point p_s corresponds to the synchronous trajectory. It is hyperbolic, parabolic or elliptic when $\mu \notin [0,4]$, $\mu \in \{0,4\}$, and $\mu \in (0,4)$, respectively. If $\mu \in (0,4)$, its characteristic multipliers are $\lambda_s = e^{i\theta}$ and $1/\lambda_s$, for some $\theta \in (0,\pi)$ such that

$$\cos\theta = 1 - \mu/2. \tag{7}$$

This means that the linear dynamics around p_s is conjugated to a rotation by angle θ. The quantity $\theta/2\pi$ is called *tune* in Accelerator Physics [2]. Nevertheless, following a standard terminology in dynamical systems, we will say that $\theta/2\pi$ is the *rotation number*. The elliptic point p_s is called (m,n)-*resonant* when $\theta = 2\pi m/n$ for some relatively prime integers m and n such that $1 \le m \le n/2$, which implies that $\lambda_s^n = 1$. Besides, n is the *order* of the resonance.

The fixed point $p_h = (-2\phi_s, 0)$ is hyperbolic for any $\mu > 0$. Indeed, if $\mu > 0$, then the linear dynamics around p_h expands the unstable direction by a factor $\lambda_h = e^h$ and contracts the stable direction by a factor $1/\lambda_h$, where the *characteristic exponent* $h > 0$ is given by $\cosh h = 1 + \mu/2$.

We look for initial conditions that give rise to particles with a bounded energy deviation from the synchronous trajectory. More precisely, we will estimate the size and the shape of

$$\mathcal{A} = \{p \in \mathbb{T}\times\mathbb{R} : (w_n)_{n\in\mathbb{Z}} \text{ is bounded}\}.$$

Here, $p = (\psi, w) \in \mathbb{T}\times\mathbb{R}$ and $p_n = (\psi_n, w_n) = f^n(p)$. This domain is called *(longitudinal) acceptance* in Accelerator Physics, and *stability domain* in dynamical systems. We will also study its connected component $\mathcal{D} \subset \mathcal{A}$ that contains p_s. The map f, its acceptance $\mathcal{A}$, and the connected component $\mathcal{D}$ depend on μ, but we will frequently omit this dependence. Otherwise, we will write f_μ, $\mathcal{A}_\mu$, and $\mathcal{D}_\mu$, respectively.

Remark 1. We have numerically checked that

$$\mathcal{A} \subset [-0.45, 0.35] \times [-0.8, 0.8], \quad \forall \mu > 0.$$

Hence, if $(\psi_n, w_n) \in \mathbb{T}\times\mathbb{R}$ is the phase-energy deviation at the nth turn of a trajectory contained in $\mathcal{A}$ and $(\tilde\psi_n, w_n) \in \mathbb{R}\times\mathbb{R}$ denotes the lift of this trajectory determined by $-\pi \le \tilde\psi_0 < \pi$, then $-\pi \le \tilde\psi_n < \pi$ for all n. This means that trajectories with bounded energy deviation, have also bounded phase deviation with respect to the synchronous one.

Our model map (6) is very similar to Chirikov's standard map, but with an extra wrinkle. It has nonzero *net flux*. Indeed, if we perform the change of variables

$$\psi + \phi_s = -\pi/2 - 2\pi x, \qquad z = w/2\pi,$$

then the map (6) becomes

$$\begin{cases} x = x_1 + z, \\ z = z_1 + \dfrac{\epsilon}{2\pi}\sin(2\pi x_1) + \lambda, \end{cases} \tag{8}$$

where $\lambda = 1$ is the *net flux* and $\epsilon = 2\pi/\cos\phi_s = \sqrt{4\pi^2 + \mu^2}$ quantifies the *amplitude* of the forcing term.

Fox and de la Llave [13] studied the stability domain of the map (8) for $0 < \lambda < 1$ and $0 < \epsilon \le 6$. We cannot take advantage of their work, because in our case $\lambda = 1$ and $\epsilon \ge 2\pi$. Nevertheless, one can compare their Figure 8(b) with our Fig. 5(left). They graph the relative size of the stability domain of the map (8) versus ϵ when $\lambda = 0.6$ and $0 \le \epsilon \le 6$. We graph the area of the stability domain of the map (6) versus μ when $0 \le \mu \le 4.5$. One can see the reduction of $\mathcal{A}$ after the fourth order resonance and the collapse of $\mathcal{D}$ at the third order resonance in both graphs. See Section 5 for more details.

Table 1
Relations among the synchronous phase $\phi_s \in \mathbb{T}$, the parameter $\mu \in \mathbb{R}$, the rotation number $\theta/2\pi$, and the characteristic exponent $h > 0$. Here, the values h_p and h_u are given by $\cosh h_p = 3$ and $\cosh h_u = 5/2$.

Relation	Local stability
$\mu = 2\pi \tan\phi_s$	$\mu \in (0, 4] \setminus \{3\}$
$\cos\theta = 1 - \pi \tan\phi_s$	$\theta \in (0, \pi] \setminus \{2\pi/3\}$
$\cosh h = 1 + \pi \tan\phi_s$	$h \in (0, h_p] \setminus \{h_u\}$

4. Local stability and two asymptotic formulas

First, we study when $p_s = (0, 0)$ is a *locally stable* fixed point. That is, we determine the values of μ for which all points enough close to p_s remain close under iteration of the map (6).

Theorem 1. *The synchronous trajectory is locally stable if and only if* $\mu \in (0, 4] \setminus \{3\}$.

We will prove this theorem in Appendix A. The range of local stability in terms of θ and h is given in Table 1.

Next, we focus on the invariant curves (ICs) surrounding the elliptic point p_s, especially on the "last" IC (LIC). LICs (and their rotation numbers) were studied in [15]. We have numerically computed LICs by using the algorithm described in [16].

A summary of the phenomena that take place when μ moves is displayed in Fig. 2. If there exist ICs around the origin, we plot some of them, the last one (the LIC), and one unbounded orbit very close to the LIC. If the origin is globally unstable, we plot suitable unbounded orbits to highlight it.

Fig. 2 shows the basic skeleton from which an expert reader can deduce the main dynamical changes. Let us describe them.

The elliptic fixed point p_s and the hyperbolic fixed point p_h merge in a parabolic point as $\mu \to 0^+$; see Fig. 2(a)–(c). This scenario corresponds to a saddle-center bifurcation [17,18]. The stable and unstable invariant curves (called *separatrices*) of the hyperbolic fixed point seem to form a small loop around the elliptic fixed point when $0 < \mu \ll 1$. See Fig. 2(c). We will see in Appendix B that, since the LIC around the elliptic point is exponentially close (in the parameter μ) to the separatrices,

$$|\mathcal{A}_\mu|, |\mathcal{D}_\mu| = 6\mu^{5/2}/5\pi^2 + O(\mu^3), \quad \text{as } \mu \to 0^+. \tag{9}$$

Therefore, both regions are almost the same when $\mu \to 0^+$. (If $\mathcal{R}$ is a subset of $\mathbb{T} \times \mathbb{R}$, then $|\mathcal{R}|$ denotes its area.)

The LIC grows in size, changes its shape, and moves away from the separatrices as μ increases; see Fig. 2(d). We reach the fourth order resonance $\theta = \pi/2$ at $\mu = 2$. The elliptic point is locally stable at this resonance, and the ICs near it look like a Latin cross, whose arms have a width of the order of the square of its length; see Fig. 2(e). The Hénon map displays exactly the same behavior at the fourth order resonance [19].

The twist coefficient (also called first Birkhoff coefficient) goes from negative to positive at $\mu = \mu_r \simeq 2.537706$ and from positive to negative at $\mu = 3$, where the third order resonance $\theta = 2\pi/3$ takes place. This is one of the two typical behaviors for the twist coefficient described in [20]. It means that the orbits around the origin rotate slower (resp., faster) as they go away from the origin when $\mu \in (0, \mu_r) \cup (3, 4)$ (resp., $\mu \in (\mu_r, 3)$). Fig. 2(g)–(i) show that behavior, since we see a three-periodic orbit near the elliptic point for both $\mu \lesssim 3$ and $\mu \gtrsim 3$.

The elliptic point is unstable at the third order resonance; see Fig. 2(h). We will prove in Appendix C that if $\mu = 3 + \epsilon$ with $0 < |\epsilon| \ll 1$, the LIC is approximately a triangle of vertices

$$\frac{\epsilon}{\pi}(1, 0), \qquad \frac{\epsilon}{\pi}(1, -3), \qquad \frac{\epsilon}{\pi}(-2, 3). \tag{10}$$

In particular,

$$|\mathcal{D}_{3+\epsilon}| = 9\epsilon^2/2\pi^2 + O(\epsilon^3), \quad \text{as } \epsilon \to 0. \tag{11}$$

The LIC grows in size and its triangular shape changes to a "banana-like" shape as the parameter moves from the third order resonance at $\mu = 3$ to the second order resonance at $\mu = 4$. The fixed point p_s is locally stable at this last resonance, and the ICs near it look like "bananas" whose width is of the order of the square of its length. See Fig. 2(k).

Finally, a period-doubling bifurcation takes place after the second order resonance. To be precise, the point p_s becomes a saddle for $\mu > 4$, being parabolic with reflection at $\mu = 4$. One then expects to find an elliptic two-periodic orbit for $\mu > 4$. The *separatrices* of the hyperbolic fixed point p_s form two small loops around the two elliptic two-periodic points. Nevertheless, the saddle p_s remains globally stable when $\mu \gtrsim 4$, since some of the ICs around p_s still persist. See Fig. 2(l).

In spite of all the above comments, the expulsion of some resonance is a more relevant phenomenon than any resonance at the elliptic fixed point, but the third order resonance. The reason is that only the first phenomenon changes drastically $\mathcal{A}$ and $\mathcal{D}$, since the second one takes place inside $\mathcal{D}$. We will check that $|\mathcal{A}|$ and $|\mathcal{D}|$ experiment a jump for each primary resonance that is thrown away. Besides, these primary jumps are smaller in $|\mathcal{A}|$ than in $|\mathcal{D}|$. However, $|\mathcal{A}|$ displays many more jumps, the secondary ones, which are related to resonances inside elliptic islands that are already outside $\mathcal{D}$.

5. Stability domain

5.1. Reversors

A map is *reversible* when each orbit is related to its time reverse orbit by a symmetry transformation, called a *reversor*. If a map is reversible, many of their periodic and homoclinic points are located on certain *symmetry lines*, and many of their invariant objects are invariant under the reversors [21]. Two paradigmatic examples of such invariant objects are ICs around elliptic points and stable and unstable invariant curves of hyperbolic points. We will use these facts to simplify some computations.

The map (6) can be written as the composition $f = r_1 \circ r_0$, where $r_0, r_1 : \mathbb{T} \times \mathbb{T} \to \mathbb{T} \times \mathbb{R}$ are the involutions

$$r_0(\psi, w) = (\psi + w, -w), \qquad r_1(\psi, w) = (\psi, \eta(\psi) - w), \tag{12}$$

and $\eta(\psi) = 2\pi(\cos\psi - 1) - \mu \sin\psi$. This means that the map f is reversible with reversors r_0 and r_1. See [22]. The symmetry lines of these reversors are their sets of fixed points; that is,

$$\begin{aligned} \mathrm{Fix}(r_0) &= \{(\psi, w) \in \mathbb{T} \times \mathbb{R} : w = 0\}, \\ \mathrm{Fix}(r_1) &= \{(\psi, w) \in \mathbb{T} \times \mathbb{R} : w = \eta(\psi)/2\}. \end{aligned} \tag{13}$$

All the ICs displayed in Fig. 2 are invariant under the reversors r_0 and r_1, and so is the stability domain $\mathcal{A}$. See Fig. 3.

In particular, if we consider the decomposition

$$\mathcal{A} = \mathcal{A}^- \cup \mathcal{A}^+, \qquad \mathcal{A}^\pm = \mathcal{A} \cap \{(\psi, w) \in \mathbb{T} \times \mathbb{R} : \pm w \geq 0\},$$

then $\mathcal{A}^\pm = r_0(\mathcal{A}^\mp)$. This halves the computational effort to find $\mathcal{A}$. The connected component $\mathcal{D}$ satisfies the same property.

The symmetry lines of any reversible map $f = r_1 \circ r_0$ have many more useful properties. Let us recall the characterization of *symmetric periodic orbits* (SPOs) given in [22]. SPOs are the periodic orbits that are invariant under both reversors r_0 and r_1. An orbit of f is an SPO if and only if it has exactly two points on $\mathrm{Fix}(r_0) \cup \mathrm{Fix}(r_1)$, in which case it has a point on each symmetry line if and only if it has odd period. We have displayed in Fig. 3 a couple of $(1, 4)$-SPOs.

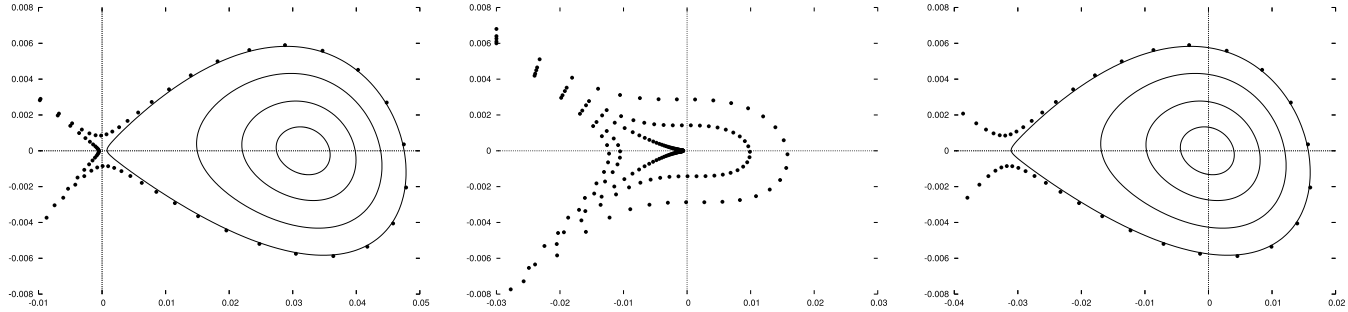

(a) ICs and two unbounded orbits for $\mu = -0.1$. (b) Five unbounded orbits for $\mu = 0$. (c) ICs and one unbounded orbit for $\mu = 0.1$.

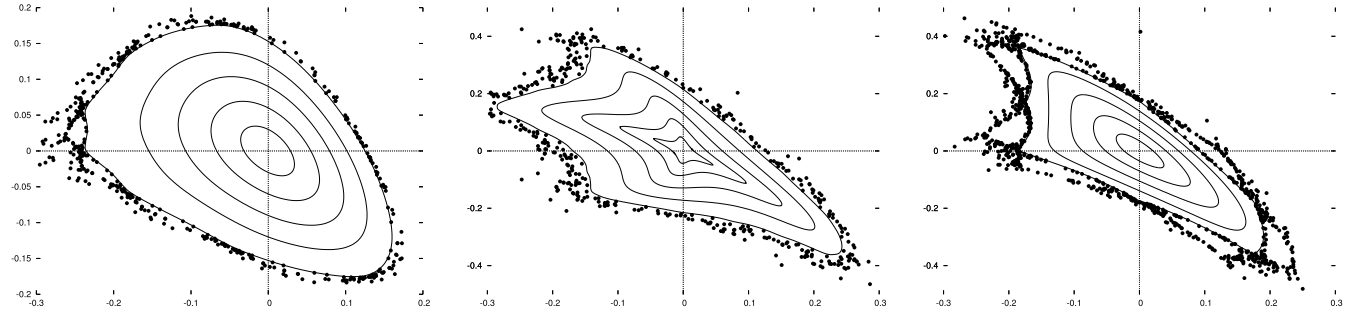

(d) ICs and one unbounded orbit for $\mu = 1$. (e) ICs and one unbounded orbit for $\mu = 2$. (f) ICs and one unbounded orbit for $\mu = \mu_r \simeq 2.53$.

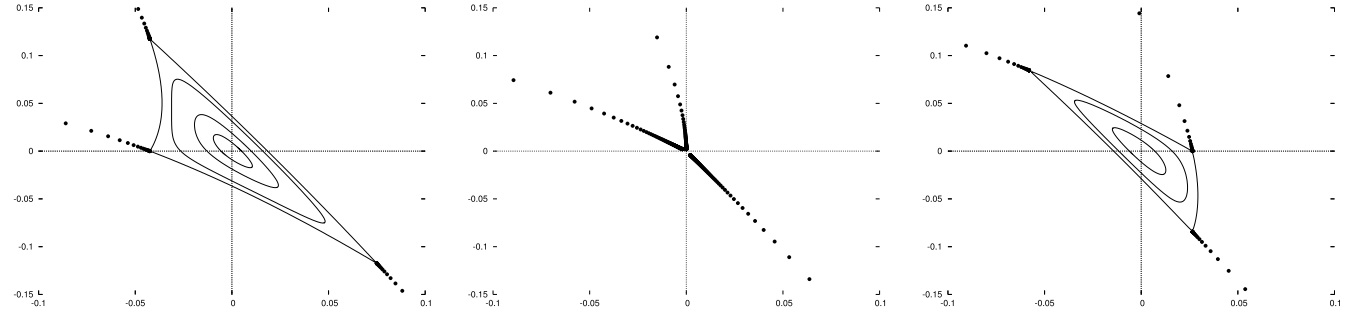

(g) ICs and one unbounded orbit for $\mu = 2.9$. (h) One unbounded orbit for $\mu = 3$. (i) ICs and one unbounded orbit for $\mu = 3.1$.

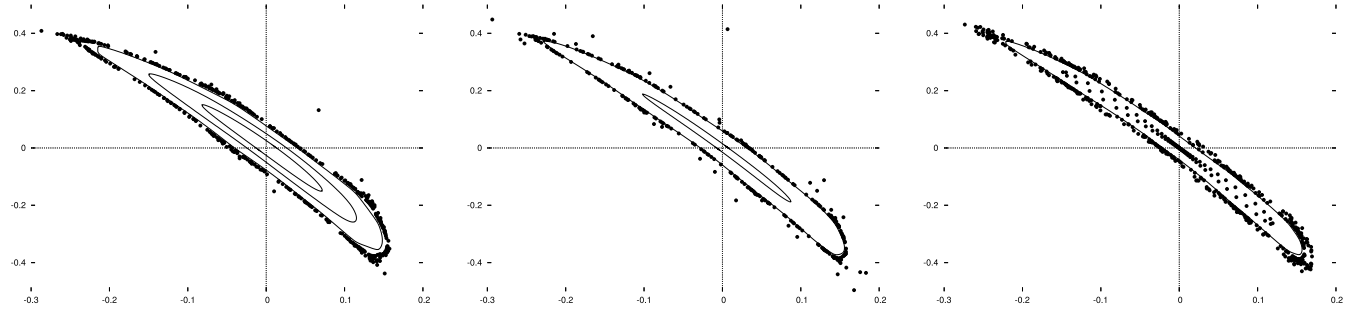

(j) ICs and one unbounded orbit for $\mu = 3.9$. (k) ICs and one unbounded orbit for $\mu = 4$. (l) One IC, one unbounded orbit and one homoclinic (to the origin) orbit for $\mu = 4.05$.

Fig. 2. Race-track microtron phase dynamics in (ψ, w)-coordinates for several values of the parameter $\mu = 2\pi \tan\phi_s$. In the electronic version one can magnify the plots to check details of the invariant curves: proximity to the unbounded orbits, regularity at their "corners", etcetera. This also applies to many other figures.

Four is even, so one of these orbits has two points on $\mathrm{Fix}(r_0)$, and the other orbit has two points on $\mathrm{Fix}(r_1)$.

5.2. Rotation number

The points inside the stability domain $\mathcal{A}$ rotate around the elliptic fixed point $p_s = (0, 0)$ when $0 < \mu < 4$. The points infinitesimally close to p_s give $\theta/2\pi$ turns per iteration, where θ is the angle defined in (7). We recall that $\theta/2\pi$ is the *rotation number* of the elliptic point p_s, and we write $\rho(p_s) = \theta/2\pi$. Next, we try to define the rotation number $\rho(p)$ for any point $p \in \mathcal{A} \setminus \{p_s\}$ following a standard approach [23].

Given any $p = (\psi, w) \in \mathcal{A}$, let φ be its "argument". That is, φ is the angle between the segment $[p_s, p]$ and the semi-straight line $\{(\psi, 0) : \psi > 0\}$. Analogously, let $\varphi_n \in \mathbb{R}$ be the "argument" of the nth iterate $p_n = f^n(p)$. We consider these arguments on the

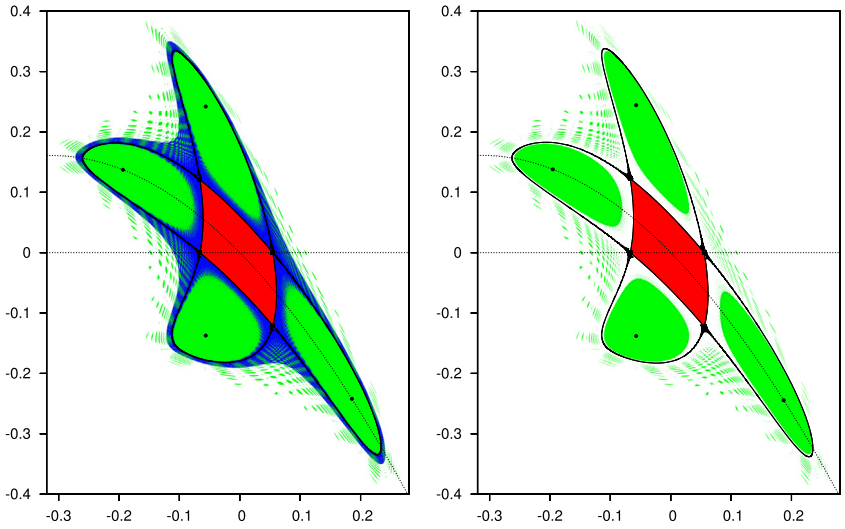

Fig. 3. The stability domain for $\mu = 2.037$ (left) and $\mu = 2.038$ (right). Blue corresponds to chaotic seas, green to periodic elliptic islands, and red to ICs. The elliptic and hyperbolic (1, 4)-SPO orbits are marked with solid black circles and solid black squares, respectively. The symmetry lines $\mathrm{Fix}(r_0)$ and $\mathrm{Fix}(r_1)$ are displayed as dashed black lines. Each SPO of even period has exactly two points on a single symmetry line. A short part of the stable and unstable invariant curves of the hyperbolic (1, 4)-SPO is drawn with continuous black lines. These stable and unstable invariant curves split (that is, they do not coincide), but only the outer splitting can be seen at this scale. See Section 6 for details. In the electronic version one can magnify the plots. (For interpretation of the references to color in this figure legend, the reader is referred to the web version of this article.)

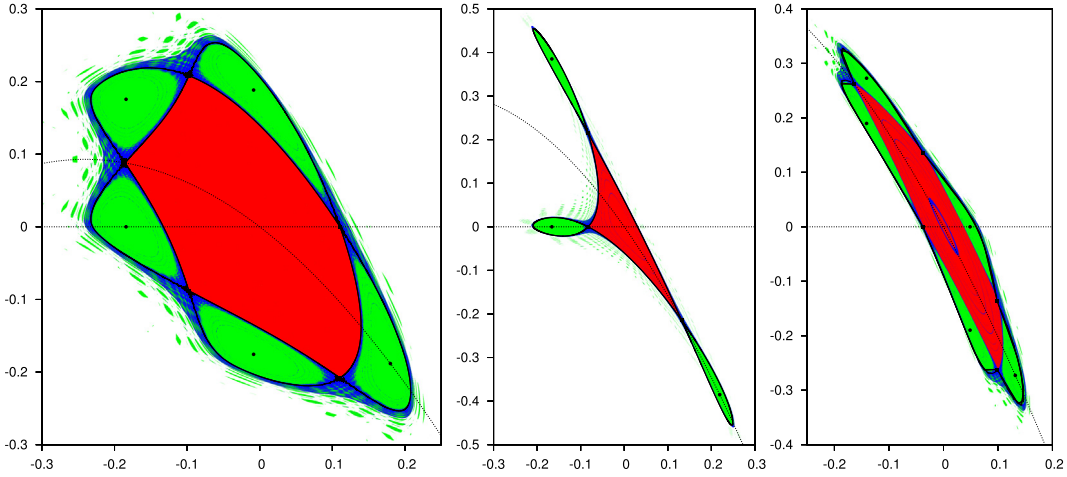

Fig. 4. The stability domain for $\mu = 1.539$ (left), $\mu = 2.853$ (center), and $\mu = 3.735$ (right). Colors, solid black circles, solid black squares, dashed black lines, and continuous black lines have the same meaning as in Fig. 3, but here the SPOs are (1, 5)-periodic (left), (1, 3)-periodic (center), and (2, 5)-periodic (right). Each SPO of odd period has exactly one point on each symmetry line. (For interpretation of the references to color in this figure legend, the reader is referred to the web version of this article.)

universal cover $\mathbb{R}$, not on $\mathbb{T} = \mathbb{R}/2\pi\mathbb{Z}$. Then we wonder whether the limit

$$\rho = \rho(p) := \frac{1}{2\pi} \lim_{n\to+\infty} \frac{\varphi_n - \varphi}{n} \tag{14}$$

exists. If so, we say that (14) is the *rotation number* of the point p under the map f around the elliptic point p_s. Such quantities can be computed using an algorithm described in [24,11].

We are interested in rotation numbers because they allow us to distinguish the three main bounded dynamical behaviors in analytic area-preserving diffeomorphisms [23,16,24]:

- If $\mathcal{C}$ is a Moser-like IC, then the limit (14) exists for all $p \in \mathcal{C}$, and it does not depend on p, so we write $\rho(\mathcal{C})$. Besides, $\rho(\mathcal{C})$ is, generically, a *Diophantine number* (that is, it is badly approximated by rational numbers).
- A (m, n)-*periodic chain of elliptic islands* is an invariant region with several connected components such that each of them surrounds a (m, n)-periodic elliptic point. The (1, 4)-periodic chain around p_s is displayed in Fig. 3 for two values of μ. It is formed by the four big green domains. Each of them is mapped onto the next one in clockwise sense, so $\rho(p) \equiv 1/4$ for any point p inside them. Similarly, if p is inside an (m, n)-periodic chain of elliptic islands, the limit (14) exists, $\rho(p) = m/n \in \mathbb{Q}$.
- A *chaotic sea* (or *Birkhoff instability zone*) is the region between two adjacent ICs minus the stable elliptic islands. If p is inside a chaotic sea, then the limit (14) generically does not exist.

From now on, we paint the points inside chaotic seas in blue, the ones inside elliptic islands in green, and the ones on ICs in red. Figs. 3 and 4 are samples of that convention. To be precise, given any point $p \in \mathcal{A}$, we apply the algorithm described in [24] to compute its rotation number. If the algorithm does not converge, then we paint p in blue. Otherwise, we paint p in red/green when $\rho(p)$ is irrational/rational, which is decided by looking at its continued fraction; see [25] for details.

5.3. Stability domain

We compute the stability domain of the microtron map (6) using the *orbit method* described in [12]. Visual examples of several

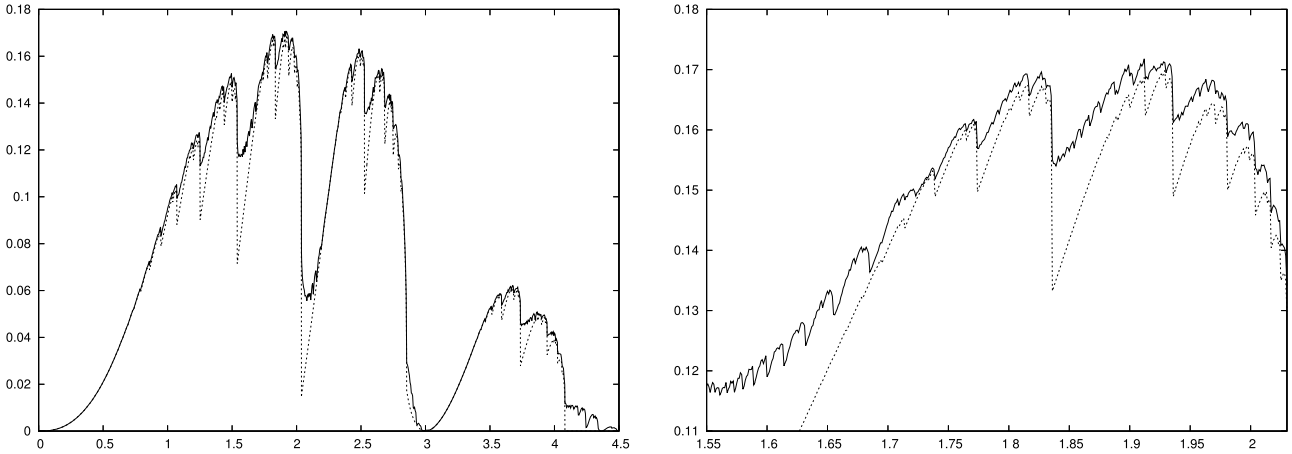

Fig. 5. Left: $|\mathcal{A}_\mu|$ (continuous line) and $|\mathcal{D}_\mu|$ (dashed line) versus μ. Right: A zoom of the previous figure to visualize its self-similar structure.

stability domains of the Hénon map provided by this method can be found in [26–28]. Our figures show a strong resemblance with those ones.

Let us describe our implementation of the orbit method.

First, we take a fine rectangular grid in a suitable rectangle

$$[\psi_{\min}, \psi_{\max}] \times [0, w_{\max}]$$

that contains the upper half $\mathcal{A}^+$ of the stability domain. Second, we paint in white all grid points such that some of their first 1000 iterates escape from the control region

$$\{(\psi, w) \in \mathbb{T} \times \mathbb{R} : |w| \leq 1\}.$$

This is a fast step, since 1000 is a relatively small number for any modern computer. Third, we consider the nth iterates with $-10^7 \leq n \leq 10^7$ of all not-yet-white grid points adjacent to some already-white one. If some of these iterates escapes from the control region, we paint in white all grid points "visited" by its corresponding unbounded orbit or by its r_0-symmetric orbit. We do not use the reversor r_1, since r_0 is computationally cheaper and $r_1 = f \circ r_0$. We repeat this process until no more points escape from the control region. This is the hardest step. Fourth, we determine the color of each non-white grid point by computing its rotation number as explained before. This step of the algorithm is not "orbitally coherent" in the sense of [12], but we feel that it is the right choice, since there is no clear way to choose the color in disputed cases. Finally, we get the lower half of the stability domain from the identity $\mathcal{A}^- = r_0(\mathcal{A}^+)$.

We stress that all grid points in the interior (respectively, "on" the border) of the stability domain have been iterated only 1000 (respectively, $2 \cdot 10^7$) times. This is good, since the interior contains much more grid points than the border.

Fig. 3 shows a couple of stability domains computed with this algorithm. Each pixel is the center of a square with side $\ell = 1/4000$, so the area of the stability domain is approximately equal to ℓ^2 times the number of colored pixels. We also count the number of pixels in the connected component containing the origin following a standard algorithm in Computer Vision. See, for instance, [30, pages. 72–75]. In that way, we obtain that $|\mathcal{A}_\mu| \approx 1.1657 \cdot 10^{-1}$ and $|\mathcal{D}_\mu| \approx 1.1029 \cdot 10^{-1}$ for $\mu = 2.037$, but $|\mathcal{A}_\mu| \approx 7.6105 \cdot 10^{-2}$ and $|\mathcal{D}_\mu| \approx 1.5067 \cdot 10^{-2}$ for $\mu = 2.038$.

These jumps in $|\mathcal{A}_\mu|$ and $|\mathcal{D}_\mu|$ have a simple explanation. We recall that the fourth order resonance takes place at $\mu = \mu_\bullet = 2$. After that value is crossed, four $(1, 4)$-periodic elliptic islands surrounded by a chaotic sea emanate from the elliptic point p_s. This structure (elliptic islands plus chaotic sea) moves away from p_s as μ grows, but remains inside $\mathcal{D}_\mu \subset \mathcal{A}_\mu$ while some IC surrounds it. However, the LIC surrounding it disappears at some value $\mu = \mu_\star \in (2.037, 2.038)$. After that value is crossed, both the elliptic islands and the chaotic sea are thrown away from the connected component $\mathcal{D}_\mu$, although any elliptic island is, by definition, part of $\mathcal{A}_\mu$. Thus, the jump in $|\mathcal{A}_\mu|$ only takes into account the loss of the chaotic sea, whereas the jump in $|\mathcal{D}_\mu|$ also takes into account the loss of many elliptic islands.

Similar jumps take place for any periodic elliptic island, although the greater is the order of the expelled island, the smaller is the jump in both areas. For instance, we see in Fig. 4 the stability domains for $\mu = 1.539$, $\mu = 2.853$, and $\mu = 3.735$, which are parameter values smaller than, but very close to, the values at which the periodic elliptic islands of orders three and five are thrown away from the connected component $\mathcal{D}$. Hence, the stability domains corresponding to $\mu = 1.540$, $\mu = 2.854$, and $\mu = 3.736$ are significantly smaller, because the more extern chaotic sea is lost.

Fig. 5 shows $|\mathcal{A}_\mu|$ and $|\mathcal{D}_\mu|$ as a function of μ. The maximal value $|\mathcal{A}_\mu| \approx 1.718 \cdot 10^{-1}$ is attained for $\mu \approx 1.912$, $|\mathcal{D}_\mu| = 0$ for all $\mu \gtrsim 4.08$, and $|\mathcal{A}_\mu| = 0$ for all $\mu \gtrsim 4.53$. Obviously, $|\mathcal{D}_\mu| \leq |\mathcal{A}_\mu|$, since $\mathcal{D}_\mu \subset \mathcal{A}_\mu$. We note that $|\mathcal{A}_\mu|$ displays many more jumps than $|\mathcal{D}_\mu|$, because it is affected by *secondary resonances* (resonances inside the islands). The graph of $|\mathcal{A}_\mu|$ has a self-similar fractal structure caused by those secondary resonances, as the displayed magnification shows.

We also list in Table 2 the exact value

$$\mu_\bullet := 2 - 2\cos(2\pi m/n) \in [0, 4] \tag{15}$$

at which the elliptic fixed point p_s becomes (m, n)-resonant, so that the (m, n)-periodic chain of elliptic islands is created from p_s, jointly with the numerically approximated value $\mu = \mu_\star$ at which the (m, n)-periodic chain of elliptic islands is thrown away from $\mathcal{D}$, for all (m, n)-resonances of order $n < 10$. For instance, the $(2, 7)$-periodic chain is thrown away at some value $\mu_\star \in (2.526, 2.527)$, which explains the seven "holes" delimited by the unbounded orbit displayed in Fig. 2(f) for $\mu_r \approx 2.538$.

We observe that $\mu_\bullet < \mu_\star$, but in the $(1, 3)$-resonance, which comes as no surprise, since the twist coefficient is positive if and only if $2.538 \approx \mu_r < \mu < 3$, see Fig. A.8.

We end with a couple of warnings regarding the accuracy of our pictures.

On the one hand, we know that the red domains displayed in Fig. 3, and in the left picture of Fig. 4 are not completely filled with ICs. Indeed, KAM theory implies that the set of all ICs has a complicated Cantorian structure, whose gaps are filled with resonances. Let us explain why we do not see those resonances. We restrict our explanation to the case of Fig. 3, since the phenomenon is the same in both cases. We do not see any resonance inside the red zone displayed in Fig. 3 because

$$\rho_\star := \rho(p_s) = \theta/2\pi = \operatorname{acos}(1 - \mu_\star/2)/2\pi \approx 0.25302,$$

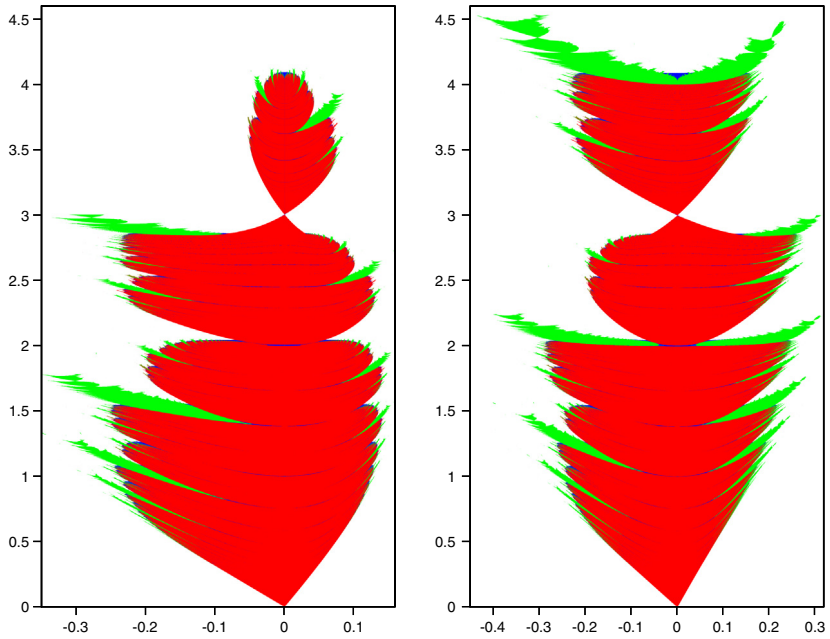

Fig. 6. The fractal sets $\mathcal{S}_0$ (left) and $\mathcal{S}_1$ (right) in the (ψ, μ)-plane. Compare with Fig. 2 in [29]. (For interpretation of the references to color in this figure legend, the reader is referred to the web version of this article.)

Table 2
Exact values $\mu_\bullet$ at which the main resonances emanate from p_s, and approximated values $\mu_\star$ at which they escape from $\mathcal{D}$.

(m, n)	Emanate at	Escape at $\mu_\star$ with
$(1, 9)$	$\mu_\bullet \approx 0.468$	$0.859 < \mu_\star < 0.860$
$(1, 8)$	$\mu_\bullet = 2 - \sqrt{2} \simeq 0.586$	$0.948 < \mu_\star < 0.949$
$(1, 7)$	$\mu_\bullet \approx 0.753$	$1.071 < \mu_\star < 1.072$
$(1, 6)$	$\mu_\bullet = 1$	$1.251 < \mu_\star < 1.252$
$(1, 5)$	$\mu_\bullet = \frac{1}{2}(5 - \sqrt{5}) \simeq 1.382$	$1.539 < \mu_\star < 1.540$
$(2, 9)$	$\mu_\bullet \approx 1.653$	$1.835 < \mu_\star < 1.836$
$(1, 4)$	$\mu_\bullet = 2$	$2.037 < \mu_\star < 2.038$
$(2, 7)$	$\mu_\bullet \approx 2.445$	$2.526 < \mu_\star < 2.527$
$(1, 3)$	$\mu_\bullet = 3$	$2.853 < \mu_\star < 2.854$
$(3, 8)$	$\mu_\bullet = 2 + \sqrt{2} \simeq 3.414$	$3.589 < \mu_\star < 3.590$
$(2, 5)$	$\mu_\bullet = \frac{1}{2}(5 + \sqrt{5}) \simeq 3.618$	$3.735 < \mu_\star < 3.736$
$(3, 7)$	$\mu_\bullet \approx 3.802$	$3.942 < \mu_\star < 3.943$
$(4, 9)$	$\mu_\bullet \approx 3.879$	$4.023 < \mu_\star < 4.024$
$(1, 2)$	$\mu_\bullet = 4$	$4.080 < \mu_\star < 4.081$

when $\mu = \mu_\star \in (2.037, 2.038)$, see Table 1. Therefore, all missed resonances have orders $n \geq 83$, since $21/83$ is the rational number in the interval $(1/4, \rho_\star)$ with the smallest denominator. Such resonances are too small to be detected with our pixel resolution. We recall that a generic (m, n)-resonance in an $O(\eta)$-neighborhood of an elliptic fixed point of an analytic area preserving map has an $O(\eta^{n/4})$-size [26].

On the other hand, the border of the connected component $\mathcal{D}_\mu$ should be a red curve (the LIC), which is missing in the left picture of Fig. 3 and in the three pictures of Fig. 4. The reason is, once more, that the LIC is too thin to be detected with our pixel resolution. In the same way, probably there are some ICs in the middle of the blue zone, which would mean that blue zone is composed by several chaotic seas, instead of by a single big chaotic sea.

5.4. Sections with the symmetry lines

We consider the sections of the stability domain with the symmetry lines (13) for two reasons. First, the stability domain is symmetric with respect to these lines. Second, we recall that each SPO has exactly two points on these lines, and such SPOs are the basic invariant objects that organize the dynamics inside their resonance.

We look at Fig. 3 to understand how SPOs organize the resonant dynamics. We see an elliptic $(1, 4)$-SPO with two points on $\mathrm{Fix}(r_1)$ that organizes the stable dynamics inside the four big green elliptic islands, and a hyperbolic $(1, 4)$-SPO with two points on $\mathrm{Fix}(r_0)$ whose stable and unstable invariant curves delimit almost perfectly the red region "filled" with ICs.

We do not deal with each one-dimensional section as a separate object, but we gather them into the two-dimensional sets:

$$\mathcal{S}_0 = \left\{(\psi, \mu) \in \mathbb{T} \times (0, +\infty) : (\psi, 0) \in \mathcal{A}_\mu\right\},$$
$$\mathcal{S}_1 = \left\{(\psi, \mu) \in \mathbb{T} \times (0, +\infty) : (\psi, \eta(\psi)/2) \in \mathcal{A}_\mu\right\},$$

in order to visualize their evolution in the parameter μ.

These sets are represented in Fig. 6 with the usual color codes. We see that the connected component $\mathcal{D}_\mu$ collapses to the elliptic fixed point at $\mu = 3$, and undergoes its major loss at some $\mu = \mu_\star \in (2.037, 2.038)$. The collapse is associated to the local instability of the third order resonance. The loss takes place when the fourth order resonance is thrown away. These are the most relevant phenomena regarding the size of the stability domain in generic families of area-preserving maps.

We appreciate a clear self-similar fractal structure in the sets $\mathcal{S}_0$ and $\mathcal{S}_1$. One can magnify their pictures to appreciate several details. Let us describe the main ones.

Resonances emanate from the elliptic fixed point p_s in the form of thin blue and green tongues, since they are sections of chaotic seas surrounding elliptic islands. These tongues begin at the points $(\psi, \mu) = (0, \mu_\bullet)$, where $\mu_\bullet$ is defined as in (15) for any rational number $m/n \in (0, 1/2)$, so there are infinitely many of such tongues. Besides, they look symmetric with respect to the vertical line $\{\psi = 0\}$ in a neighborhood of that line. The resonances, but the $(1, 4)$-one, have a small width when they are close to p_s. Hence, most of the tongues become visible only at some distance of $\{\psi = 0\}$.

The elliptic islands inside a resonance grow in size when they move away from p_s. If the resonance has even order, then the green part becomes the biggest part of the tongue in the set $\mathcal{S}_1$, but not in the set $\mathcal{S}_0$. This means that each elliptic SPO with even period has

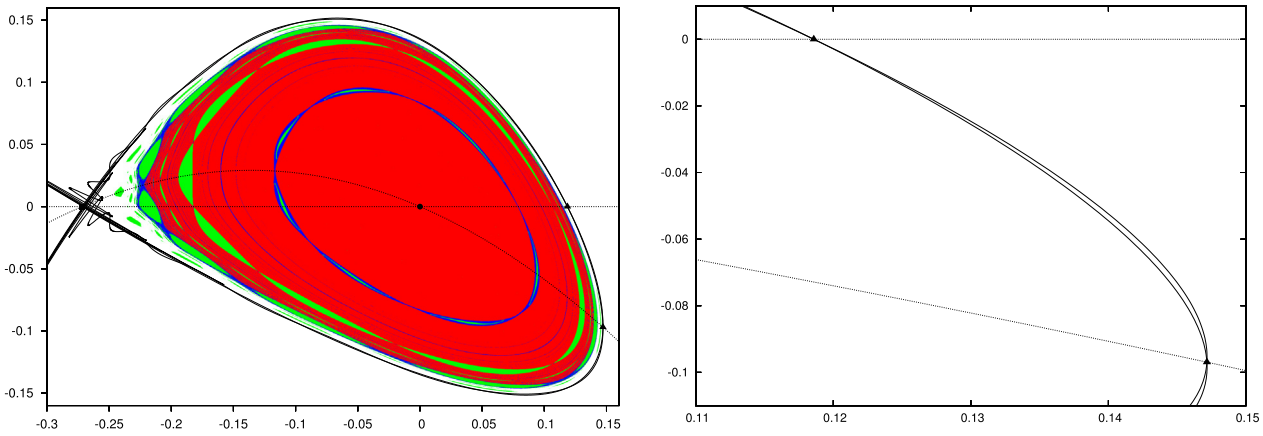

Fig. 7. Left: The stability domain for $\mu = 0.859$. Blue corresponds to chaotic seas, green to periodic elliptic islands, and red to ICs. The elliptic fixed point $p_s = (0, 0)$ and the hyperbolic fixed point $p_h = (-2\phi_s, 0)$ are marked with a solid black circle and a solid black square, respectively. The symmetry lines Fix(r_0) and Fix(r_1) are displayed as dashed black lines. A short part of the stable and unstable invariant curves of p_h is shown as continuous black lines. The primary intersections of these invariant curves with the symmetry lines are marked with two solid black triangles. Right: A zoom of the left figure, but without the stability domain. The area of the lobe $\mathcal{L}$ delimited by the separatrices between the two primary homoclinic points marked with solid black triangles is $|\mathcal{L}| \approx 3.808194826948494 \times 10^{-5}$. (For interpretation of the references to color in this figure legend, the reader is referred to the web version of this article.)

two points on Fix(r_1), but none on Fix(r_0). Fig. 3 is a sample of that empirical claim. On the contrary, if the resonance has odd order, then the green part becomes the biggest part of just one branch of the tongue, in both sets $\mathcal{S}_0$ and $\mathcal{S}_1$. The other branch remains blue. This is a completely expected behavior, since we know that all SPOs with odd period have just one point on each symmetry line.

We warn that red and green regions should not be in direct contact, but we have again difficulties to detect the blue chaotic seas between them with our current pixel resolution.

Resonances are thrown away from $\mathcal{D}$, which is the reason for the saw-like border of $\mathcal{S}_0$ and $\mathcal{S}_1$. Once a green tongue is separated from the main red body in the ψ-direction, it is no longer delimited by blue portions, because chaotic seas do not form part of $\mathcal{A}$ when their resonances are thrown away. See Fig. 3. Besides, the separated part of any green tongue shows a shape similar to the shape of the whole set, which is due to the secondary resonances. Indeed, we see the two above-mentioned phenomena (major loss in the stability domain and collapse of the stability domain to a point) along many of these tongues.

Such phenomena are clearly visible in the tongues of $\mathcal{S}_1$ that cover the range $4.08 < \mu < 4.53$. The fixed point p_s is already globally unstable in that range, but there is still a locally stable elliptic two-periodic orbit on the symmetry line Fix(r_1).

Hénon studied some sets similar to $\mathcal{S}_0$ and $\mathcal{S}_1$ for the Hénon map more than forty years ago [29]. His computations already show many of the above-described phenomena, in spite of the limitations of the computers in that time. Such limitations were recently overcome in [31].

6. On the invariant curves of some hyperbolic points

The stable and unstable invariant curves of hyperbolic (fixed or periodic) points organize the dynamics of area preserving maps in several ways. For instance, some of these invariant curves are approximate boundaries of stability domains [32], and the flux through certain closed curves composed by arcs of invariant curves can be easily computed [33]. Such flux is exponentially small area in the analytic case [34], so that the above-mentioned closed curves become *partial barriers* of the dynamics [35,33]. If the map is entire, then the stable and unstable invariant curves never coincide [36], so these partial barriers are never complete barriers. Next, we discuss these ideas in the setting of map (6).

6.1. Singular splitting near the saddle-center bifurcation

We will see in Appendix B that the map (6) is approximated, after the rescaling (B.1), by the $\mu^{1/2}$-time flow of the Hamiltonian (B.2) when $0 < \mu \ll 1$. Besides, the Hamiltonian (B.2) has a separatrix that encloses a region which resembles the stability domain of the map when $0 < \mu \ll 1$. Compare the stability domain displayed in Fig. 2(c) with the phase portrait of the Hamiltonian (B.2) sketched in Fig. B.10. The separatrix is described by the homoclinic trajectory (B.3), which is analytic in a complex strip of width $d_0 = \pi$.

Nevertheless, the stable and unstable invariant curves of the saddle point $p_h = (-2\phi_s, 0)$ of our map (6) do not coincide, since the map is entire. This result goes back to Ushiki [36]. We have displayed the stability domain and the separatrices of the saddle point $p_h = (-2\phi_s, 0)$ for $\mu = 0.859$ in Fig. 7 (left). The separatrices enclose the stability domain. The reversibility of our map implies that the separatrices have a primary homoclinic point on each symmetry line (13). Let $\mathcal{L}$ be the region (such region is called *lobe*) delimited by the pieces of the separatrices between these two primary homoclinic points. For instance, we display the lobe $\mathcal{L}$ for $\mu = 0.859$ in Fig. 7 (right). In that case, the lobe area is $|\mathcal{L}| \approx 3.808194826948494 \times 10^{-5}$.

Fontich and Simó [34] proved that the splitting of the separatrices for any close to the identity analytic area preserving map is exponentially small in the characteristic exponent h of the saddle point. To be precise, they established that the splitting size is smaller than $O(e^{-2\pi d/h})$ for any $0 < d < d_0 = \pi$. Here, d_0 is the width of the analyticity strip of the homoclinic solution of the limit Hamiltonian. Since in our case $d_0 = \pi$, we get the upper bound $|\mathcal{L}| \leq O(e^{-c/h})$ for any $0 < c < 2\pi^2$. We recall that $\mu = 2(\cosh h - 1) = h^2 + O(h^4)$, so $h \asymp \sqrt{\mu}$ as $\mu \to 0^+$.

Ten years later, Gelfreich [18] derived an asymptotic formula for the splitting angle between the separatrices in analytic saddle-center bifurcations, although he did not provide a complete proof. Gelfreich's formula, once adapted to our map, says that $|\mathcal{L}| \asymp a_0 e^{-2\pi^2/h}$ as $h \to 0^+$ for some constant $a_0 \in \mathbb{R}$.

Our numerical experiments strongly suggest that there exist some asymptotic coefficients $a_n \in \mathbb{R}$, $n \geq 0$, such that

$$|\mathcal{L}| \asymp e^{-2\pi^2/h} \sum_{n\geq 0} a_n h^{2n}, \quad (h \to 0). \tag{16}$$

This fits perfectly with both Fontich–Simó's upper bound, and Gelfreich's asymptotic formula. Our refined asymptotic formula (16)

means that if we retain only finitely many terms of the right-hand side, then the error will be of the order of the first discarded term. Such refined asymptotic formulas in singular splitting problems were first presented in [37] for the Standard map, and first proved in [38] for the perturbed McMillan map.

Besides, we have numerically seen that the first asymptotic coefficient in formula (16) is non-zero:

$$a_0 \approx 1.420985027091898137266172597 27 \times 10^5,$$

whereas the second asymptotic coefficient vanishes: $a_1 = 0$, so the approximation $|\mathcal{L}| \approx a_0 e^{-2\pi^2/h}$ has an $O(h^4)$ relative error. We have also checked that the asymptotic series $\sum_{n\geq 0} a_n h^{2n}$ is divergent, but its Borel transform $\sum_{n\geq 0} a_n h^{2n}/(2n)!$ has radius of convergence $2\pi^2$. This is a typical behavior for many other maps, see [39–41,31].

Let us consider the closed curve formed by the unstable invariant curve from the saddle point p_h to the primary homoclinic point on some fixed symmetry line plus the stable invariant curve from that primary point to p_h. This closed curve encloses a planar domain $\mathcal{R}$ slightly bigger than the stability domain $\mathcal{A}$, see Fig. 7 (left). The key observation is that this closed curve is an *effective barrier* when $0 < \mu \ll 1$. The term *effective* means that the flux through this closed curve is so small that it looks like a true barrier for a very big number of iterates of the map. For instance, if we set $\mu = 0.2$, then $h \approx 0.44357$,

$$|\mathcal{R}| > |\mathcal{A}| \approx 2.1455 \times 10^{-3},$$

$$|\mathcal{L}| \approx a_0 e^{-2\pi^2/h} \approx 6.7000 \times 10^{-15}.$$

Besides, we know that the lobe area $|\mathcal{L}|$ is an exact measure of the flux through $\partial\mathcal{R}$ after one iteration of the map, see [35,33]. This means that after 10^9 iterates of the map f, less than three thousandths parts of the points inside $\mathcal{R}$ have escaped. Thus, one may approximate the stability domain $\mathcal{A}$ by the region $\mathcal{R}$ in many practical situations.

Finally, we note that the numerical computation of any exponentially small splitting quantity (angle, area, or distance) gets complicated by problems of precision, stability, and time. In order to overcome them, Simó proposed to use a multiple-precision arithmetic, to expand the invariant curves up to high order, and to take advantage of the reversor [42]. These ideas have been used in [39–41]. We have also used them.

6.2. Singular splitting near the third-order resonance

We will see in Appendix C that the third power of map (6) is approximated, after the rescaling (C.1), by the ϵ-time flow of the Hamiltonian (C.2) when $\mu = 3 + \epsilon$ with $0 < |\epsilon| \ll 1$. Besides, the Hamiltonian (C.2) has three saddle points whose invariant curves coincide giving rise to the triangle sketched in Fig. C.12.

If $\mu \simeq 3$, then the stability domain of the map (6) has a central part with a triangular shape, that contains many ICs, and three "sheets", that contain points with rotation number equal to 1/3, attached to the vertices of that "triangle". The vertices of this "triangle" correspond to hyperbolic three-periodic points whose stable and unstable invariant curves do not coincide. There are two different splitting phenomena in this setting. Namely, the inner splitting (associated to the invariant curves that enclose the "triangle") and the outer splitting (associated to the invariant curves that enclose the "sheets"). Each splitting should be studied separately. The inner one is generically much smaller than the outer one [26].

We have displayed the stability domain for $\mu = 2.853$ in the central picture of Fig. 4. The red part is the "triangle", the green parts are the three "sheets", and the continuous black lines are the invariant curves of the hyperbolic three-periodic points. We stress that, although the value of $|\epsilon| = |\mu - 3|$ is not very small, the inner splitting cannot be detected even after a big magnification of our picture. This suggest that the inner splitting is exponentially small in $|\epsilon| = |\mu - 3|$. G. Moutsinas [43] has studied the inner splitting in analytic area-preserving maps close to the third-order resonance. He deduced, under a generic assumption on the third-order Birkhoff normal form around the elliptic fixed point at the exact third-order resonance, that the inner splitting is exponentially small in the characteristic exponent of the third iterate of the map at the hyperbolic three-periodic points. To be more precise, he found that the Lazutkin homoclinic invariant (a celebrated splitting quantity introduced in [44]) associated to some distinguished heteroclinic orbits has a refined asymptotic formula of the form (16), but now h is the characteristic exponent of the map f^3 at the three-periodic points instead of the characteristic exponent of the map f at the origin.

On the contrary, the outer splitting in the central picture of Fig. 4 can be perceived after a suitable magnification of a small neighborhood of a hyperbolic three-periodic point. This visual inspection fits with the results given in [26, Section 6.1], where it is established that the outer splitting associated to a generic third-order resonance does not tend to zero as we approach the resonance. That is, the outer splitting is $O(1)$.

We can extract two practical consequences of these results.

First, set $\mu \simeq 3$ and let $\mathcal{R}^{(1,3)}_{\text{inner}}$ and $\mathcal{R}^{(1,3)}_{\text{outer}}$ be the regions enclosed by suitable parts of the stable and unstable invariant curves of the hyperbolic three-periodic points such that $\mathcal{R}^{(1,3)}_{\text{inner}}$ contains the triangular shaped part of $\mathcal{A}$ containing many ICs and $\mathcal{R}^{(1,3)}_{\text{outer}}$ contains all the points with rotation number equal to 1/3. Then the flux through the effective barrier $\partial\mathcal{R}^{(1,3)}_{\text{inner}}$ is much smaller than the flux through $\partial\mathcal{R}^{(1,3)}_{\text{outer}}$.

Second, let $\mu_\star \in [2.853, 2.854]$ be the value at which the third-order resonance is thrown away from $\mathcal{D}$. Then $\mathcal{R}^{(1,3)}_{\text{inner}}$ is a really good approximation of the connected component $\mathcal{D}$ when $\mu \gtrsim \mu_\star$.

6.3. Singular splitting near high-order resonances

The singular splitting near resonances of order $n \geq 4$ shares several qualitative and quantitative features with the singular splitting near the saddle-center bifurcation and near the third-order resonance. Let us explain this.

Let $\mu_\bullet$ and $\mu_\star$ be the values at which the (m, n)-resonance emanates from p_s and is thrown away from $\mathcal{D}$, respectively. Let $\mathcal{R}^{(m,n)}_{\text{inner}}$ (respectively, $\mathcal{R}^{(m,n)}_{\text{outer}}$) be the region enclosed by suitable parts of the inner (respectively, enclosed between suitable parts of the inner and outer) branches of the stable and unstable invariant curves of the hyperbolic (m, n)-periodic points. The inner region usually looks like a red "polygon" with n curved sides, because it is almost completely foliated by ICs, whereas the outer region contains the (m, n)-periodic chain of elliptic islands, and it also contains part of its surrounding chaotic sea before the (m, n)-resonance is thrown away. See Figs. 3 and 4 for several pictures about the resonances

$$(m, n) = \{(1, 4), (1, 5), (1, 3), (2, 5)\}.$$

Since the flux through the borders of the inner and outer regions can be geometrically interpreted as the area of certain lobes [35,33], we obtain the following information about the inner and outer flux. The inner flux is smaller than the outer flux, and both of them are exponentially small in $|\mu - \mu_\bullet|$ [26]. The inner region is a good approximation of the connected component $\mathcal{D}$ when $\mu \gtrsim \mu_\star$. See, for instance, the right picture in Fig. 3. The inner and outer regions are not completely contained in the stability domain when $\mu > \mu_\star$, since there is a small, but not zero, flux through their borders [36].

7. Discussion of results and conclusions

We have studied the stability of longitudinal beam motion in RTMs within a model that was previously considered in [9,45,2]. Oscillations of particle energy and accelerating field phase, usually called phase oscillations, with respect to the same parameters of a reference particle referred to as synchronous particle, are described by the area preserving map (6). Though the model assumes a few approximations, discussed in Section 2 and summarized at the end of the present section, it captures important features of the phase oscillations both in circular microtrons and in RTMs and allows to obtain the main characteristics of the longitudinal beam dynamics. In fact, similar models are widely used for design and characterization of other types of particle accelerators [46].

We have analyzed the stability domain $\mathcal{A}$ (and its central connected component $\mathcal{D}$) of the area-preserving map (6) that describes the phase oscillations. We have studied their structure and calculated their area as a function of ϕ_s. We have combined various approaches, theorems, and tools of dynamical systems. To the best of our knowledge, the study of the stability domain of the map (6) carried out here is the most complete and detailed. It is an essential widening and improvement of results reported in [45,2], in which either the power expansion of the map up to the cubic order in terms of the phase space variables or numerical simulations with low number of turns were used.

The knowledge of $\mathcal{A}$, called longitudinal acceptance in the theory of particle accelerators, is of much importance for the optimization of the beam motion in RTMs. Indeed, the adjustment of machine parameters for the efficient acceleration of the beam during its commissioning consists in matching the domain in the phase space occupied by the particles emitted by an injector (often an electron gun) to the acceptance for a given value of ϕ_s. The optimal beam matching allows to minimize beam losses and undesired excess of strayed radiation produced by the accelerator and, so, maximize the output beam current without increasing the current at the injection. For the adjustment to be most efficient, the acceptance area must be maximal and the shape of the phase domain of the injected beam must fit the acceptance shape. Thus, a detailed description of the acceptance geometry is useful for the design of particle accelerators, especially in the case of microtrons for which the nonlinear effects in the longitudinal beam dynamics are quite strong.

The results obtained here are not meant to be directly used in the design of future RTMs or operation of existing ones. Nevertheless, a few examples of their relation to real accelerators can be mentioned. In particular, let us comment on two "empirical" rules used in microtrons [2] that can be justified with our results. The first rule claims that the values of ϕ_s for which an accelerator can operate are contained in the interval of linear stability of the synchronous trajectory. The second rule states that the optimal values of ϕ_s are close to the middle point of such interval. (We recall that $\mu = 2\pi \tan\phi_s$.) We have checked that both rules are in fact quite precise within our RTM model, where the interval of linear stability is $(0, \phi_p)$, with

$$\phi_p := \arctan(2/\pi) \approx 32.5^\circ.$$

First, we have numerically seen that $|\mathcal{D}| > 0$ for $0 < \phi_s < 33^\circ$, except for the value

$$\phi_u := \arctan(3/2\pi) \approx 25.5^\circ$$

that corresponds to the third order resonance. Second, we have found that the acceptance area reaches its maximal value $|\mathcal{A}| \approx 0.17$ at $\mu \approx 1.912$, which roughly corresponds to

$$\phi_s \approx \arctan(1.912/2\pi) \approx 16.9^\circ \approx \phi_p/2.$$

In fact, $|\mathcal{A}|$ is sufficiently large for a rather wide range of the values of μ. For instance, $|\mathcal{A}| \geq 0.1$ if

$$\mu \in [1.027, 1.071] \cup [1.079, 2.037] \cup [2.245, 2.827].$$

We have seen that $|\mathcal{A}| > 0$ up to $\mu \approx 4.53$ (that is, $\phi_s \approx 35.8^\circ$), that exceeds the value $\mu = 4$ (that is, $\phi_s \approx 32.5^\circ$), usually considered as a limit in design calculations of a microtron.

The sizes of $\mathcal{A}$ and $\mathcal{D}$ along the ψ and w axes are important for the beam matching. If the beam is previously bunched around ϕ_s then the bunch length in ψ must be shorter than the corresponding size of the acceptance and the energy dispersion around $E_{n,s}$ measured in terms of w – see (5) – must be smaller than its size in this variable. For example, let us consider the case $\mu = 2$. Then $\Delta\psi = \psi_{\max} - \psi_{\min} \approx 0.55$ and $\Delta w = w_{\max} - w_{\min} \approx 0.8$. See Fig. 2(e). The bunches at the injection should fit the region with the sizes $\Delta\psi$ and Δw in order to avoid beam losses during the acceleration (in practice, to minimize beam losses). This means that

$$\left|\frac{E_0 - E_{0,s}}{\Delta_s}\right| < 0.12$$

and $\Delta l \lesssim 0.1\lambda$, where Δl is the bunch length and λ is the wavelength of the accelerating RF field.

In the case of small accelerators there is no buncher and the beam is produced by an electron gun which emits particles continuously, so that they occupy the whole interval $[0, 2\pi]$ in the phase variable ψ at the AS entrance. Our results provide an estimate of the beam capture efficiency ϵ; that is, the fraction of the initial beam that is successfully accelerated. If $\mu = 2$, then

$$\epsilon = \frac{\Delta\psi}{2\pi} \approx 0.09.$$

Our numerical computations show that $\epsilon \leq 0.13$ for all μ in the RTM model. See Remark 1 in Section 3. This result gives the theoretical upper bound on the capture efficiency in RTMs with high number of turns. One should however keep in mind that in real machines the beam makes only a few turns, so the capture efficiency is usually higher.

We have studied the reduction of $|\mathcal{D}|$ in the vicinity of resonant values. For instance, $|\mathcal{D}| = 0$ at the third order resonance $\phi_s = \phi_u$, whereas $|\mathcal{D}| \approx 0.02$ after the fourth order resonance

$$\phi_s = \arctan(1/\pi) \approx 17.7^\circ.$$

Other resonances do not lead to so sharp decreases of $|\mathcal{D}|$. This data is quite important because one of the criteria of choosing the design value of ϕ_s is to avoid values close to resonant ones. Otherwise even a small natural drift of machine parameters may lead to ϕ_s approaching one of the dangerous resonant values and consequently to excessive beam losses. In this respect, the asymptotic formulas (9) and (11) are of much interest. Another important aspect of the acceptance structure is the elliptic islands and chaotic seas like the ones displayed in Figs. 3–4. For instance, each drastic change in $|\mathcal{D}|$ is associated to the escape of a chain of elliptic islands from $\mathcal{D}$.

The structure of the stability domain with periodic elliptic islands suggests an interesting possibility of beam acceleration in different parts of the phase space. Such idea, that would require a quite detailed knowledge of the stability domain geometry, was already mentioned in the literature (see [2] and references therein), however no RTM design with such acceleration scheme has been proposed so far.

We know very few experimental data that can be compared with the results obtained in the present paper. Characteristics of practical importance in microtrons are the number of accelerated particles, or the beam current which is directly proportional to the area of the stability region, and the effective voltage in the

accelerating structure which is inversely proportional to $\cos\phi_s$. The area of the stability region varies with the synchronous phase ϕ_s according to the plot in Fig. 5. On the one hand, similar plots obtained by numerical simulations for a small number of turns (less than 30) were published in [9,45,2]. On the other hand, the current–voltage characteristic was measured experimentally in a microtron with 30 orbits [47]. The experimental results, once expressed in the variables (μ, current), show a good qualitative agreement with Fig. 5, though some quantitative differences exist. For instance, a dip in the current–voltage characteristic that should correspond to the third order resonance does not reach zero value as for the theoretical curve in Fig. 5. The difference is explained by a quite low number of beam turns in the experiment and by measurement errors. The dip becomes more profound as the observed number of turns grows [47].

Another interesting phenomena that was observed in operation of microtrons [48] is a two-humped distribution of the electron bunch in the transverse direction for $\mu \gtrsim 2$; that is, close to the fourth order resonance. It was observed repeatedly in experiments by a few groups [1]. Such bunch structure can be explained by the presence of four periodic elliptic islands of the stability domain displayed in Fig. 3. See a discussion in [45].

In our study the stability is understood in the mathematical sense. That is, we are dealing with perpetual stability, although only $2 \cdot 10^7$ turns were considered in our numerical computations of $\mathcal{A}$. Nevertheless, the number of turns made by each particle is typically of just a few tens in real RTMs. For instance, the number of turns is roughly 90 in the RTM machine of the MAMI complex at the Institute for Nuclear Physics in Mainz, which is nowadays the largest RTM facility in operation [49]. Thus, the physical acceptance and the true capture efficiency are larger than the mathematical stability domain and the estimates of ϵ given above, respectively. In fact, as the comparison with the experimental measurement of the current–voltage characteristic discussed above shows, the difference may not be that large because in many cases the beam instability develops quite rapidly, after just a few iterations.

We have studied the case of the multiplicity increase factor $k = 1$, see Section 2. The general case $k \in \mathbb{N}$ can be analyzed in a similar way, and the stability domains turn out to be smaller.

We have assumed that the acceleration gap is of zero length and that the velocity of particle is equal to the speed of light already at the injection. The latter is not the case for compact RTMs with the injection from a standard electron gun. It would be useful to develop an approach in which these conditions are relaxed. A finite-size accelerating gap can be taken into account by introducing a transit-time factor [46]. The non-relativistic dynamics, which is of practical importance for the design of small low-energy RTMs, can be considered by a corresponding modification of map (6); see [14].

We have modeled the magnetic field in the RTM end magnets by a simplified hard-edge distribution, without taking into account neither the fringe field effect [46] nor more complicated field profiles [5]. Studying the longitudinal dynamics in these cases is also of interest for the RTM beam physics.

In our study we have assumed that electrons do not lose energy due to the synchrotron radiation. Simple estimates show that the energy loss per turn grows cubically in the number of turns, but remains very small in the first turns. Therefore, the effect of synchrotron radiation can be neglected for practical applications. For example, for the compact RTM described in [4] it turns out that the energy loss due to synchrotron radiation per turn is less that 1% of the energy gain per turn Δ_s in the first five hundred turns when $\Delta_s = 2$ MeV.

Finally, let us note that in our study the phase oscillations of particles of the beam were considered as independent of the transverse oscillations, vertical and horizontal. This approximation is valid if the amplitudes of these oscillations are small.

Appendix A. Proof of Theorem 1

If $\mu \notin [0, 4]$, then p_s is hyperbolic, and so, locally unstable.

If $\mu = 0$, then the map (6) has the form

$$\begin{cases} w_1 = w - \pi(\psi + w)^2 + \mathrm{O}_4(\psi, w), \\ \psi_1 = \psi + w. \end{cases}$$

On the other hand, the Levi-Civita criterion [50] implies that the origin is unstable under any analytic map of the form

$$\begin{cases} w_1 = w + \mathrm{O}_2(\psi, w), \\ \psi_1 = \psi + w + \mathrm{O}_2(\psi, w), \end{cases}$$

with $\frac{\partial^2 w_1}{\partial \psi^2}(0, 0) \neq 0$. In our concrete map, $\frac{\partial^2 w_1}{\partial \psi^2}(0, 0) = -2\pi \neq 0$. Thus, the synchronous trajectory is locally unstable if $\mu = 0$.

If $\mu = 2$, then the map (6) takes the form

$$\begin{cases} \psi_1 = \psi + w, \\ w_1 = -2\psi - w - a(\psi_1), \end{cases}$$

where $a(\psi_1) = 2\pi(1 - \cos\psi_1) - 2(\psi_1 - \sin\psi_1) = \mathrm{O}(\psi_1^2)$. We consider the area preserving linear change of variables

$$x = \psi + w, \qquad y = \psi,$$

which transforms the previous map into

$$\begin{pmatrix} x_1 \\ y_1 \end{pmatrix} = \begin{pmatrix} -y - a(x) \\ x \end{pmatrix} = R_{\pi/2} \begin{pmatrix} x \\ y + a(x) \end{pmatrix}. \tag{A.1}$$

Let $\sum_{j \geq 2} a_j x^j$ be the Taylor expansion of $a(x)$. We know from Corollary 4.2 in [10] that if $a_2 \neq 0$ and $a_3 \neq 0$, then the origin is locally unstable under the analytic map (A.1) if and only if

$$0 < a_3 \leq a_2^2.$$

In our concrete map, $a_2 = \pi$ and $a_3 = -1/3$. Therefore, the synchronous trajectory is locally stable when $\mu = 2$.

If $\mu = 3$, then the map (6) takes the form

$$\begin{cases} \psi_1 = \psi + w, \\ w_1 = -3\psi - 2w - \pi(\psi + w)^2 + \mathrm{O}_3(\psi, w). \end{cases}$$

The map $(\psi_3, w_3) = f^3(\psi, w)$ is close to the identity, since

$$\begin{cases} \psi_3 = \psi - \pi(3\psi^2 + 2\psi w) + \mathrm{O}_3(\psi, w), \\ w_3 = w + \pi(6\psi^2 + 6\psi w + w^2) + \mathrm{O}_3(\psi, w). \end{cases}$$

We determine the local stability of the origin under the map f^3 (and so, under the map f) by applying Simó's criterion [10]. That criterion states that the origin is locally stable under an analytic area preserving map of the form

$$\begin{cases} x_1 = x + \mathrm{O}_2(x, y), \\ y_1 = y + \mathrm{O}_2(x, y), \end{cases}$$

if and only if $G(x_1, y)$ has a strict extremum at the origin, where $x_1 y + G(x_1, y)$ is the generating function of the map; that is, $G(x_1, y)$ is a function determined by the implicit equations

$$x_1 = x + \frac{\partial G}{\partial y}(x_1, y) \quad \text{and} \quad y_1 = y - \frac{\partial G}{\partial x_1}(x_1, y).$$

Thus, we look for a function $G(w_3, \psi) = O_3(w_3, \psi)$ such that

$$w_3 = w + \frac{\partial G}{\partial \psi}(w_3, \psi) \quad \text{and} \quad \psi_3 = \psi - \frac{\partial G}{\partial w_3}(w_3, \psi).$$

After a straightforward computation, we obtain that

$$G(w_3, \psi) = \pi\psi(\psi + w_3)(2\psi + w_3) + \mathrm{O}_4(\psi, w_3).$$

This function has no strict extremum at the origin. Therefore, the synchronous trajectory is locally unstable when $\mu = 3$.

If $\mu = 4$, then the map (6) takes the form

$$\begin{cases} \psi_1 = \psi + w, \\ w_1 = -4\psi - 3w + b(\psi_1), \end{cases}$$

where $b(\psi_1) = 2\pi(\cos\psi_1 - 1) + 4(\psi_1 - \sin\psi_1) = O(\psi_1^2)$. We consider the area preserving linear change of variables

$$x = 2\psi + w, \qquad y = \psi,$$

which transforms the previous map into

$$\begin{cases} x_1 = -x + b(x - y), \\ y_1 = x - y. \end{cases} \tag{A.2}$$

Let $\sum_{j\geq 2} b_j u^j$ be the Taylor expansion of $b(u)$. We know from Lemma 1.4 in [10] that if $b_2 \neq 0$, $b_3 \neq 0$, and $2b_3 + b_2^2 > 0$, then the origin is locally stable under the analytic map (A.2). In our concrete map, $b_2 = -\pi$ and $b_3 = 2/3$. Therefore, the synchronous trajectory is locally stable when $\mu = 4$.

Finally, we consider the generic case $\mu \in (0, 4) \setminus \{2, 3\}$. If $\lambda_s = e^{i\theta}$ is the characteristic multiplier of the elliptic point p_s, then $\lambda_s^n \neq 1$ for any integer n such that $1 \leq n \leq 4$; see Table 1. Therefore, p_s is not a *strongly resonant* elliptic point and the map (6) can be put into its third order *Birkhoff normal form*

$$z_1 = e^{i(\theta + \tau|z|^2)} z + O(|z|^4), \tag{A.3}$$

for some real coefficient τ, called *first Birkhoff coefficient* or *twist coefficient*. After some tedious computations [51], one gets the expression

$$\tau(\theta) = \frac{2\cos^3\theta - 3\cos^2\theta + 4\pi^2\cos\theta + 1 + \pi^2}{(\cos\theta - 1)(2\cos\theta + 1)\sin^2\theta}. \tag{A.4}$$

We observe that $\lim_{\theta\to 0^+} \theta^4\tau(\theta)$, $\lim_{\theta\to 2\pi/3}(\theta - 2\pi/3)\tau(\theta)$, and $\lim_{\theta\to\pi^-}(\theta - \pi)^2\tau(\theta)$ exist and are negative. That is, $\tau(\theta)$ has a negative fourth-order pole at $\theta = 0$, a negative simple pole at $\theta = 2\pi/3$, and a negative second-order pole at $\theta = \pi$. These properties agree with the generic behavior of twist coefficients of families of area-preserving maps described in [20].

Consequently, we deduce that $\tau(\theta)$ has at least one root in the interval $(0, 2\pi/3)$. Let us prove that it has no more real roots. The numerator in (A.4) is the polynomial $a\zeta^3 + b\zeta^2 + c\zeta + d$ in the variable $\zeta = \cos\theta$, with $a = 2$, $b = -3$, $c = 4\pi^2$, and $d = 1 + \pi^2$. This cubic polynomial has one real root and two complex conjugated roots, because its discriminant is negative:

$$\Delta = b^2c^2 - 4ac^3 - 4b^3d - 27a^2d^2 + 18abcd \simeq -536135.$$

This means that $\tau(\theta)$ has just one root θ_r in the interval $(0, \pi)$. It was numerically computed in [51] that

$$\theta_r \simeq 1.8429983434122 \in (0, 2\pi/3).$$

We have plotted the twist coefficient τ versus θ in Fig. A.8.

Finally, we recall that the Moser twist theorem [52] implies that the origin is a stable elliptic fixed point of any analytic map of the form (A.3) when $\tau \neq 0$. Hence, the synchronous trajectory is locally stable when $\theta \in (0, \pi) \setminus \{\pi/2, \theta_r, 2\pi/3\}$; or, equivalently, when $\mu \in (0, 4) \setminus \{2, \mu_r, 3\}$, where

$$\mu_r = 2 - 2\cos\theta_r \simeq 2.5377060556582.$$

If $\mu = \mu_r$, then the third order Birkhoff normal form (A.3) does not provide much information because the first Birkhoff coefficient $\tau_1 = \tau$ vanishes. Thus, we should compute the fifth order Birkhoff normal form

$$z_1 = e^{i(\theta_r + \tau_1|z|^2 + \tau_2|z|^4)} z + O(|z|^6),$$

where $\tau_1 = 0$ and $\tau_2 \in \mathbb{R}$ is the *second Birkhoff coefficient*. The analytical computation of τ_2 is cumbersome, so we have taken a simpler numerical approach. First, we have computed the rotation number $\rho(p)$ of the points of the form $p = (\psi, 0)$. Next, we have checked that

$$\rho(\psi, 0) = \theta_r/2\pi + \rho_2\psi^4 + O(\psi^5), \tag{A.5}$$

for some non-zero coefficient $\rho_2 \approx -200$, which implies that $\tau_2 \neq 0$. Then the Moser twist theorem implies that the origin is a stable elliptic fixed point [52].

The flat behavior (A.5) is clearly observed in Fig. A.9. The small gaps that appear in the graph correspond to the sections of some chaotic seas with the symmetry line $\mathrm{Fix}(r_0) = \{w = 0\}$. The rotation number is not well defined on those sections.

This completes the proof of Theorem 1.

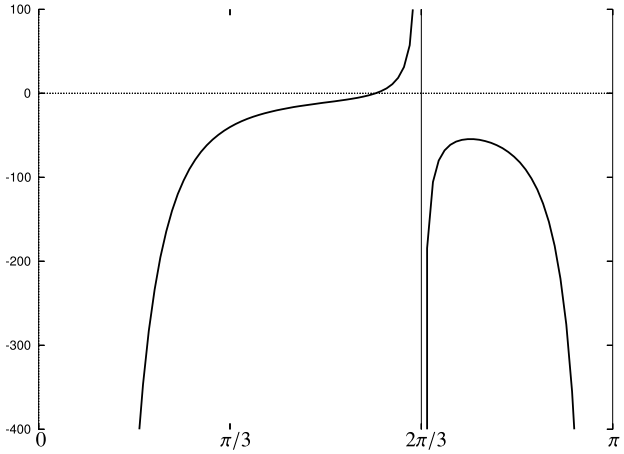

Fig. A.8. The twist coefficient τ versus θ.

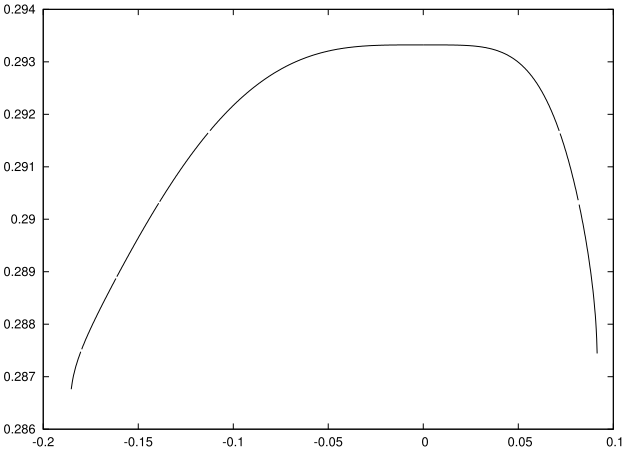

Fig. A.9. The rotation number $\rho(\psi, 0)$ versus ψ for $\mu = \mu_r$.

Appendix B. Proof of the asymptotic formula (9)

Let us study the size and shape of $\mathcal{D}_\mu \subset \mathcal{A}_\mu$ when $\mu \to 0^+$.

The elliptic fixed point $p_s = (\psi_s, 0) = (0, 0)$ and the hyperbolic fixed point $p_h = (\psi_h, 0)$ of the map (6) collapse as $\mu \to 0^+$. The following rough quantitative estimates are typical for saddle-center bifurcations. The size of $\mathcal{A}_\mu$ in the ψ-coordinate is $O(|\psi_s - \psi_h|) = O(\mu)$. Its size in the w-coordinate is $O(|\psi_s - \psi_h|) \times O(\mu^{1/2}) = O(\mu^{3/2})$, since the angle between the eigenvectors of the matrix M_h is $O(\mu^{1/2})$. Consequently, $\mathcal{A}_\mu = O(\mu) \times O(\mu^{3/2}) = O(\mu^{5/2})$. Finally, $|\mathcal{A}_\mu| \asymp |\mathcal{D}_\mu|$ when $\mu \to 0^+$. We will confirm and refine these rough estimates.

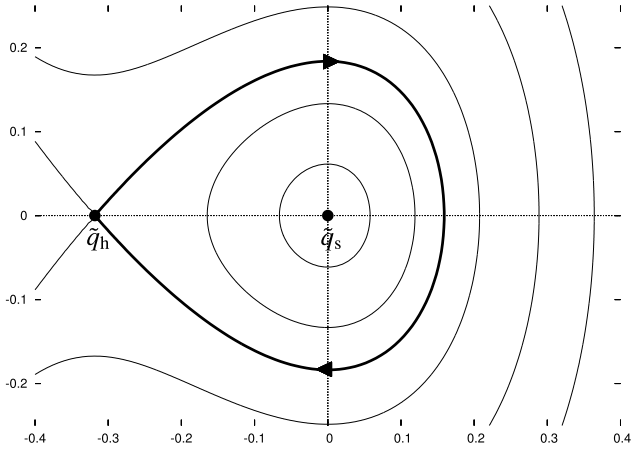

Fig. B.10. The separatrix (thick line), some level curves (thin lines), and the two equilibrium points (small circles) of the limit Hamiltonian (B.2) associated to the saddle-center bifurcation. The black arrows show the Hamiltonian dynamics on the separatrix.

Following the above comments, we scale the ψ-coordinate (respectively, w-coordinate) by a factor of order μ (respectively, order $\mu^{3/2}$). To be precise, we consider the change of scales

$$x = \psi/\mu, \qquad y = w/\mu^{3/2}. \tag{B.1}$$

If $0 < \mu \ll 1$, then the map (6) is transformed under this change into a map $(x_1, y_1) = \tilde{f}(x, y)$ of the form

$$\begin{cases} x_1 = x + \mu^{1/2} y, \\ y_1 = y - \mu^{1/2}(x + \pi x^2) + \mathrm{O}(\mu). \end{cases}$$

The map $\tilde{f}$ is close to the identity map $\mathrm{I}(x, y) = (x, y)$, since

$$\tilde{f} = \mathrm{I} + \mu^{1/2}\tilde{f}_1 + \mathrm{O}(\mu), \qquad \tilde{f}_1(x, y) = (y, -x - \pi x^2).$$

The term $\tilde{f}_1$ is a Hamiltonian vector field with Hamiltonian

$$\tilde{H}_1(x, y) = \frac{x^2 + y^2}{2} + \frac{\pi}{3}x^3 - \frac{1}{6\pi^2}. \tag{B.2}$$

We have subtracted the constant $1/6\pi^2$ for convenience. We denote by ϕ_H^t the t-time flow of a Hamiltonian H. Then

$$\tilde{f} = \mathrm{I} + \mu^{1/2}\tilde{f}_1 + \mathrm{O}(\mu) = \phi_{\tilde{H}_1}^{\mu^{1/2}} + \mathrm{O}(\mu) = \phi_{\mu^{1/2}\tilde{H}_1}^{1} + \mathrm{O}(\mu),$$

since the Euler method has a second order local truncation error.

Therefore, the integrable dynamics of the Hamiltonian $\tilde{H}_1$ approximates the dynamics of the map $\tilde{f}$ in the limit $\mu \to 0^+$. We say that $\tilde{H}_1$ is the *limit Hamiltonian* associated to the saddle-center bifurcation. It has two equilibrium points. Namely, the elliptic point $\tilde{q}_s = (0, 0)$ and the saddle point $\tilde{q}_h = (-1/\pi, 0)$. Besides, the unstable and stable invariant curves of the saddle point coincide along one branch, giving rise to the separatrix

$$\tilde{\mathcal{S}} = \left\{ \tilde{q} = (x, y) \in \mathbb{R}^2 : \tilde{H}_1(\tilde{q}) = 0,\ x > -1/\pi \right\}.$$

Let $\tilde{\mathcal{R}}$ be the domain enclosed by $\tilde{\mathcal{S}} \cup \{\tilde{q}_h\}$. The phase portrait of Hamiltonian (B.2) is sketched in Fig. B.10. Only points inside $\tilde{\mathcal{R}}$ give rise to bounded trajectories, so $\tilde{\mathcal{R}}$ is a good approximation of the scaled versions of $\mathcal{A}_\mu$ and $\mathcal{D}_\mu$ when $0 < \mu \ll 1$.

The separatrix $\tilde{\mathcal{S}}$ is described by a homoclinic trajectory $\tilde{q}(t) = (x(t), y(t))$ to the saddle point: $\lim_{t\to\pm\infty} \tilde{q}(t) = \tilde{q}_h$. If we impose the initial condition $y(0) = 0$ and solve the Hamiltonian equations on the separatrix $\tilde{\mathcal{S}}$, we get that

$$x(t) = \frac{3}{2\pi\cosh^2(t/2)} - \frac{1}{\pi}, \qquad y(t) = \frac{3\sinh(t/2)}{2\pi\cosh^3(t/2)}. \tag{B.3}$$

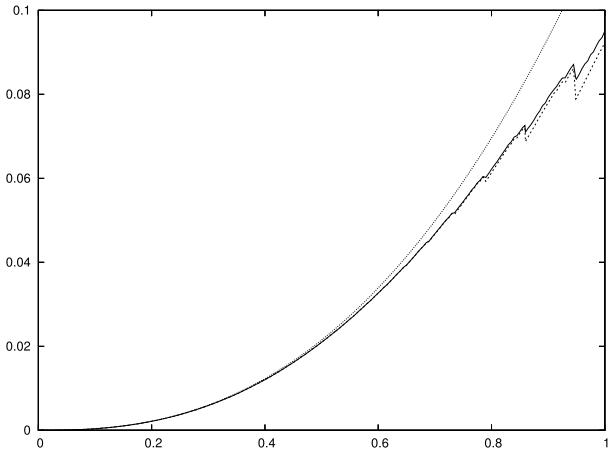

Fig. B.11. $|\mathcal{A}_\mu|$ (continuous line), $|\mathcal{D}_\mu|$ (dashed line), and the asymptotic estimate $6\mu^{5/2}/5\pi^2$ (dotted line) versus μ.

Therefore, $|\tilde{\mathcal{R}}| = \oint_{\tilde{S}} y\mathrm{d}x = \int_{-\infty}^{+\infty} y(t)x'(t)\mathrm{d}t = 6/5\pi^2$. The first identity follows from Green's theorem, the last one follows from the residue's theorem. The asymptotic estimate (9) follows from the change of scales (B.1).

Fig. B.11 shows a strong agreement between the numerically computed values of $|\mathcal{A}_\mu|$ and $|\mathcal{D}_\mu|$ and their asymptotic estimate $\mu \mapsto 6\mu^{5/2}/5\pi^2$, even for relatively big values of μ.

Appendix C. Proof of the asymptotic formula (11)

Let us study the size and shape of the connected component $\mathcal{D}_\mu$ of the acceptance when $\mu = 3 + \epsilon$ with $0 < |\epsilon| \ll 1$. We will see that $\mathcal{D}_{3+\epsilon}$ is approximately a triangle of vertices (10), which implies that the asymptotic estimate (11) holds. We scale the variables according to these claims, which suggest that all the interesting dynamics takes place in a $O(\epsilon)$-neighborhood of the origin. To be precise, we consider the change of scale

$$x = \pi\psi/\epsilon, \qquad y = \pi w/\epsilon. \tag{C.1}$$

If $\mu = 3 + \epsilon$ with $|\epsilon| \ll 1$, then the map (6) is transformed under this change into a map $(x_1, y_1) = \tilde{f}(x, y)$ of the form

$$\begin{cases} x_1 = x + y, \\ y_1 = -3x - 2y - x_1(x_1 + 1)\epsilon + \mathrm{O}(\epsilon^2). \end{cases}$$

The map $\tilde{f}^3$ is close to the identity: $\tilde{f}^3 = \mathrm{I} + \epsilon\tilde{f}_1 + \mathrm{O}(\epsilon^2)$, with

$$\tilde{f}_1(x, y) = (3x + 2y - 3x^2 - 2xy, -6x - 3y + 6x^2 + 6xy + y^2).$$

The term $\tilde{f}_1$ is a Hamiltonian vector field with Hamiltonian

$$\tilde{H}_1(x, y) = (1 - x)(x + y - 1)(2x + y + 1). \tag{C.2}$$

Therefore, $\tilde{f}^3 = \phi_{\epsilon\tilde{H}_1}^1 + \mathrm{O}(\epsilon^2)$, and the integrable dynamics of the Hamiltonian $\tilde{H}_1$ approximates the dynamics of the map $\tilde{f}^3$ when $\mu \simeq 3$. Thus, $\tilde{H}_1$ is the *limit Hamiltonian* associated to the third order resonance. It has four equilibrium points. One elliptic point: $\tilde{q}_s = (0, 0)$, and three saddle points:

$$\tilde{q}_1 = (1, 0), \qquad \tilde{q}_2 = (1, -3), \qquad \tilde{q}_3 = (-2, 3).$$

Let $\tilde{\mathcal{R}}$ be the triangle whose vertices are these three points. Clearly, $|\tilde{\mathcal{R}}| = 9/2$. Each side of $\tilde{\mathcal{R}}$ is both the stable invariant curve of a saddle, and the unstable invariant curve of another saddle. That is, $\partial\tilde{\mathcal{R}}$ is formed by the three saddles and the three straight separatrices connecting them. See Fig. C.12.

Only the points inside $\tilde{\mathcal{R}}$ give rise to bounded trajectories, so $\tilde{\mathcal{R}}$ is a good approximation of the scaled version of $\mathcal{D}_\mu$ for

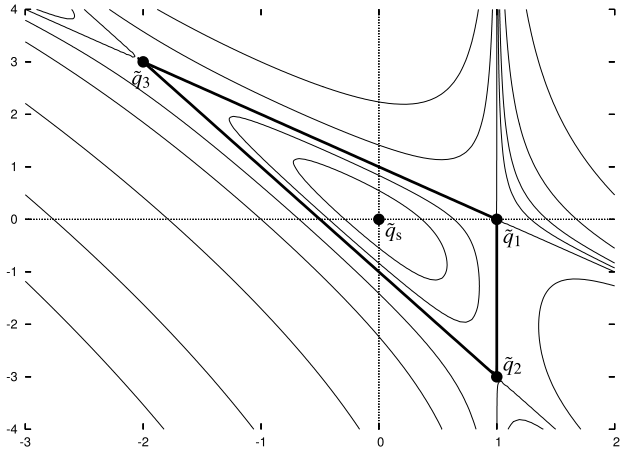

Fig. C.12. The three separatrices (thick lines), some level curves (thin lines), and the four equilibrium points (small circles) of the limit Hamiltonian (C.2) associated to the third order resonance.

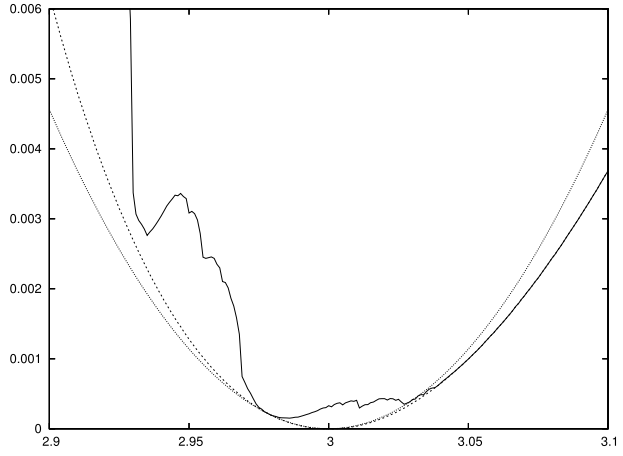

Fig. C.13. $|\mathcal{A}_\mu|$ (continuous line), $|\mathcal{D}_\mu|$ (dashed line), and the asymptotic estimate $9(\mu-3)^2/2\pi^2$ (dotted line) versus the parameter μ.

$\mu \simeq 3$. Thus, we get the quadratic asymptotic estimate (11). We have displayed a comparison between $|\mathcal{D}_{3+\epsilon}|$ and its asymptotic estimate $9\epsilon^2/2\pi^2$ in Fig. C.13. We note that $|\mathcal{A}_3| > 0$, because of the traces of the (1, 3)-periodic chain of elliptic islands that was thrown away from the main connected component $\mathcal{D}_\mu$ at some value $\mu_\star \approx 2.85$. We visualized these traces in Fig. 6.

References

[1] S.P. Kapitza, V.N. Melekhin, The Microtron, Harwood Academic Publishers, 1978.
[2] R.E. Rand, Recirculating Electron Accelerators, Harwood Academic Publishers, 1984.
[3] A.V. Aloev, D. Carrillo, Yu.A. Kubyshin, N.I. Pakhomov, V.I. Shvedunov, Electron gun with off-axis beam injection for a race-track microtron, Nucl. Instrum. Methods A 624 (2010) 39–46.
[4] Yu.A. Kubyshin, et al. Current status of the 12 MeV UPC race-track microtron, in: C. Petit-Jean-Genaz, ed., Proc. PAC-2009 (Vancouver, Canada, 2009), pp. 2775–2779.
[5] I.Y. Vladimirov, N.I. Pakhomov, V.I. Shvedunov, Y.A. Kubyshin, J.P. Rigla, V.V. Zakharov, End magnets with rare earth permanent magnet material for a compact race-track microtron, Eur. Phys. J. Plus 129 (2014) 171.
[6] V.I. Veksler, A new method of acceleration of relativistic particles, J. Phys. 9 (1945) 153–158.
[7] P. Lidbjörk, Microtrons, in S. Turner, ed., Fifth General Accelerator Physics Course (CERN, 2001) pp. 971–981.
[8] C. Henderson, F.F. Heyman, R.E. Jennings, Phase stability of the microtron, Proc. Phys. Soc. B 66 (1953) 41–49.
[9] V.N. Melekhin, Theory of nonlinear difference equations and resonance instability in phase oscillations in a microtron and of oscillations of rays in open resonators, Sov. Phys. JETP 34 (1972) 702–708.
[10] C. Simó, Stability of degenerate fixed points of analytic area preserving mappings, Astérisque (1982) 98–99. Soc. Math. France, Paris.
[11] A. Luque, J. Villanueva, Quasi-periodic frequency analysis using averaging-extrapolation methods, SIAM J. Appl. Dyn. Sist. 13 (2013) 1–46.
[12] A. Vieiro, Study of the effect of conservative and weakly dissipative perturbations on symplectic maps and Hamiltonian systems (Ph.D. Thesis), Universidad de Barcelona, 2009.
[13] A.M. Fox, R. de la Llave, Barriers to transport and mixing in volume-preserving maps with nonzero flux, Physica D 295–296 (2015) 1–10.
[14] Yu.A. Kubyshin, A.P. Poseryaev, V.I. Shvedunov, Longitudinal beam dynamics with phase slip in race-track microtrons, Nucl. Instrum. Methods A 596 (2008) 147–156.
[15] J.M. Mackay, J. Stark, Locally most robust circles and boundary circles for area-preserving maps, Nonlinearity 5 (1992) 867–888.
[16] C. Simó, D.V. Treschev, Evolution of the last invariant curve in a family of area preserving maps, preprint 1998.
[17] H. Broer, R. Roussarie, C. Simó, Invariant circles in the Bogdanov-Takens bifurcation for diffeomorphisms, Ergodic Theory Dynam. Systems 16 (1996) 1147–1172.
[18] V.G. Gelfreich, Splitting of a small separatrix loop near the saddle-center bifurcation in area-preserving maps, Physica D 136 (2000) 266–279.
[19] C. Simó, Invariant Curves Near Parabolic Points and Regions of Stability, in: Lecture Notes in Math., 819, Springer, Berlin, 1980, pp. 418–424.
[20] R. Moeckel, Generic bifurcations of the twist coefficient, Ergodic Theory Dynam. Systems 10 (1990) 185–195.
[21] R.L. Devaney, Reversible diffeomorphisms and flows, Trans. Amer. Math. Soc. 218 (1976) 89–113.
[22] J.S.W. Lamb, J.A.G. Roberts, Time-reversal symmetry in dynamical systems: A survey, Physica D 112 (1998) 1–39.
[23] A. Katok, B. Hasselblatt, Introduction to the Modern Theory of Dynamical Systems, Cambridge Univ. Press, 1995.
[24] T.M. Seara, J. Villanueva, On the numerical computation of Diophantine rotation numbers of analytic circle maps, Physica D 217 (2006) 107–120.
[25] A.Ya. Khinchin, Continued Fractions, The University of Chicago Press, 1964.
[26] C. Simó, A. Vieiro, Resonant zones, inner and outer splittings in generic and low order resonances of area preserving maps, Nonlinearity 22 (2009) 1191–1245.
[27] C. Simó, A. Vieiro, Dynamics in chaotic zones of area preserving maps: Close to the separatrix and global instability zones, Physica D 240 (2011) 732–753.
[28] C. Simó, A. Vieiro, Some remarks on the abundance of stable periodic orbits inside homoclinic lobes, Physica D 240 (2011) 1936–1953.
[29] M. Hénon, Numerical study of quadratic area-preserving mappings, Quart. Appl. Math. 27 (1969) 291–312.
[30] L. Shapiro, G. Stockman, Computer Vision, Prentice-Hall, 2002.
[31] N. Miguel, C. Simó, A. Vieiro, From the Hénon conservative map to the Chirikov standard map for large parameter values, Regul. Chao. Dyn. 18 (2013) 469–489.
[32] M. Giovannazzi, Stability domain of planar symplectic maps using invariant manifolds, Phys. Rev. E 53 (1996) 6403–6412.
[33] J.D. Meiss, Symplectic maps, variational principles, and transport, Rev. Modern Phys. 64 (1992) 795–848.
[34] E. Fontich, C. Simó, The splitting of separatrices for analytic diffeomorphisms, Ergodic Theory Dynam. Systems 10 (1990) 295–318.
[35] R.S. MacKay, J.D. Meiss, I.C. Percival, Transport in Hamiltonian systems, Physica D 13 (1984) 55–81.
[36] S. Ushiki, Sur les liaisons-cols des systèmes dynamiques analytiques, C. R. Acad. Sci., Paris Ser. A 291 (1980) 447–449.
[37] V.G. Gelfreich, V.F. Lazutkin, N.V. Svanidze, A refined formula for the separatrix splitting for the standard map, Physica D 71 (1994) 82–101.
[38] P. Martín, D. Sauzin, T.M. Seara, Exponentially small splitting of separatrices in the perturbed McMillan map, Discrete Contin. Dyn. Syst. 31 (2011) 301–372.
[39] A. Delshams, R. Ramírez-Ros, Singular separatrix splitting and the Melnikov method: An experimental study, Exp. Math. 8 (1999) 29–48.
[40] R. Ramírez-Ros, Exponentially small separatrix splittings and almost invisible homoclinic bifurcations in some billiard tables, Physica D 210 (2005) 149–179.
[41] V. Gelfreich, C. Simó, High-precision computations of divergent asymptotic series and homoclinic phenomena, Discrete Contin. Dyn. Syst. 10 (2008) 681–698.
[42] C. Simó, Analytical and numerical computation of invariant manifolds, in: D. Benest, C. Froeschlé (Eds.), Modern Methods in Celestial Mechanics, Editions Frontières, Gif-sur-Yvette, 1990, pp. 285–330.
[43] G. Moutsinas, Splitting of separatrices in area-preserving maps close to 1 : 3 resonance (Ph.D. Thesis), U. Warwick, 2016.
[44] V.G. Gelfreich, V.F. Lazutkin, M.B. Tabanov, Exponentially small splittings in Hamiltonian systems, Chaos 1 (1991) 137–142.
[45] V.N. Melekhin, Phase dynamics of particles in a microtron and the problem of stochastic instability of nonlinear systems, Sov. Phys. JETP 41 (1976) 803–808.
[46] H. Wiedemann, Particle Accelerator Physics, Springer, 2003.
[47] V.N. Melekhin, L.B. Luganskii, High-current microtron instability, Sov. Phys.-Tech. Phys. (1970) 1930–1931.
[48] V.P. Bykov, Investigation of electron bunches in a microtron, Sov. Phys. JETP 13 (1961) 1169–1174.
[49] A. Jankowiak, et al. Commissioning and operation of the 1.5 GeV Harmonic Double Sided Microtron at Mainz University, in: C. Petit-Jean-Genaz, ed., Proc. EPAC-2008 (Genoa, Italy, 2008), pp. 51–55.
[50] T. Levi-Civita, Sopra alcuni criteri di instabilità, Ann. Mat. Ser. III 5 (1901) 221–307.
[51] O. Larreal, Cálculo de la escisión de separatrices y regiones de estabilidad usando precisión múltiple: El microtrón y la singularidad Hopf-cero (Ph.D. Thesis), U. Politècnica de Catalunya, 2011.
[52] C.L. Siegel, J.K. Moser, Lectures on Celestial Mechanics, Springer-Verlag, 1995.